The Astrophysical Journal, 997:44 (29pp), 2026 January 20 https://doi.org/10.3847/1538-4357/ae12a0

Abundance of Heavy *r*-process Elements in CEMP-rs Stars: The Role of the *i*-process

A. M. Riyas[1], D. Karinkuzhi[1,2], S. Van Eck[2,3], A. Choplin[2,3], S. Goriely[2,3], L. Siess[2,3], M. V. Keerthy[1], A. Jorissen[2,3], and T. Merle[2,4]
[1] Department of Physics, University of Calicut, Thenhipalam, Malappuram, Kerala 673635, India
[2] Institut d'Astronomie et d'Astrophysique, Université Libre de Bruxelles, ULB, Campus Plaine C.P. 226, Boulevard du Triomphe, 1050 Bruxelles, Belgium
[3] BLU-ULB, Brussels Laboratory of the Universe, Université Libre de Bruxelles, 1050 Bruxelles, Belgium
[4] Royal Observatory of Belgium, Avenue Circulaire 3, 1180 Brussels, Belgium
Received 2025 June 9; revised 2025 October 10; accepted 2025 October 10; published 2026 January 16

Abstract

Carbon-enhanced metal-poor (CEMP) stars are ancient stars enriched in carbon and heavy elements. Some of these stars exhibit enhanced *s*-process and/or *r*-process elements, and hence are classified as CEMP-s, CEMP-rs, or CEMP-r. This classification is challenging due to the limited availability of heavy element abundances, particularly among *r*-process elements. Heavy *r*-process elements such as terbium, holmium, thulium, ytterbium, lutetium, tantalum, and iridium have rarely been measured because their sensitive lines are located in the ultraviolet. However, they provide sensitive diagnostics of the *s*-, *r*-, and *i*- nucleosynthetic processes. In this work, we aim to obtain a secure classification of CEMP-s and -rs stars and investigate whether the *i*-process can account for the measured abundance patterns in CEMP-rs stars. We derive the abundance profiles, notably for 12 heavy r-elements, including, in some cases, tantalum, using high-resolution UVES spectra of 17 CEMP-s and -rs stars. Based on indicators such as the [s/r] abundance ratio or the model-independent "abundance distance", nine stars are confirmed as CEMP-rs and six as CEMP-s. The classification of two objects remains uncertain. The *i*-process satisfactorily reproduces the abundance patterns of CEMP-rs stars. However, larger samples are needed to confirm trends with metallicity and clarify how CEMP-rs stars differ from CEMP-s stars.

Unified Astronomy Thesaurus concepts: Chemical abundances (224); Stellar nucleosynthesis (1616); Asymptotic giant branch stars (2100); Binary stars (154)

1. Introduction

The chemical abundance profiles of metal-poor stars, which formed in the early history of the galaxy, offer valuable insights into the nature and efficiency of nucleosynthesis processes that occurred in the past, as well as insight concerning the chemical evolution of the galaxy.

A significant proportion, estimated to be around 20% at [Fe/H] < -2.0 and increasing to about 30% or more at [Fe/H] < -3.0, of the stars in the halo of the Milky way have been discovered to be metal-poor as well as heavily enriched in carbon ([C/Fe] > 1.0; S. Rossi et al. 1999; S. Lucatello et al. 2006; V. M. Placco et al. 2014; J. Yoon et al. 2016; Y. S. Lee et al. 2017). They are called carbon-enhanced metal-poor stars (CEMP; T. C. Beers & N. Christlieb 2005). The CEMP stars are further classified into CEMP-r, CEMP-s, and CEMP-rs stars, depending on whether they are enriched in elements produced by the rapid neutron-capture-process (*r*-process), or the slow neutron-capture process (*s*-process) or whether they display a hybrid r+s abundance profile. The classification is mainly based on the abundances of two heavy elements, Ba (representative of the *s*-process) and Eu (representative of the *r*-process); however, the precise classification varies within studies (T. C. Beers & N. Christlieb 2005; K. Jonsell et al. 2006; T. Masseron et al. 2010; C. Abate et al. 2016; D. Karinkuzhi et al. 2021, hereafter K21). In the following, we denote as *mainly-s elements* or *mainly-r elements* those produced dominantly (i.e., by more than 50%) by, respectively, the *s*- or the *r*-process in the solar system, as defined in S. Goriely (1999).

The astrophysical origin of *s*-process elements is rather well identified, primarily in AGB stars (M. Busso et al. 1999; F. Käppeler et al. 2011). In addition, rotating massive stars have been proposed as viable contributors to the *s*-process (U. Frischknecht et al. 2016; A. Choplin et al. 2018; M. Limongi & A. Chieffi 2018) and related chemical evolution models (G. Cescutti et al. 2013; N. Prantzos et al. 2018; F. Rizzuti et al. 2021), while the nucleosynthesis site(s) of the *r*-process is still debated. The very high neutron flux required for the *r*-process is identified to originate from astrophysical sites such as mergers involving neutron stars and/or black holes (J. M. Lattimer et al. 1977; C. Freiburghaus et al. 1999; S. Goriely et al. 2011; D. Martin et al. 2015; B. P. Abbott et al. 2017; M. R. Drout et al. 2017; D. Watson 2019), core-collapse supernovae (G. J. Mathews & J. J. Cowan 1990; J. C. Wheeler et al. 1998; Y. Ishimaru et al. 2004; K. Farouqi et al. 2010), collapsars (D. M. Siegel et al. 2019), and magnetohydrodynamically driven supernovae (C. Winteler et al. 2012; N. Nishimura et al. 2015, 2017). However, the direct observational evidence has been available only for the *r*-process site associated with the neutron star mergers. The enhancement of *r*-process elements among old metal-poor stars is a definite sign that the *r*-process took place early in the Galactic history (C. Sneden et al. 2008; F. K. Thielemann et al. 2017). The variations in abundances shown by different stellar populations, especially at lower metallicities, indicate the need for two or more astrophysical sites for the production of *r*-process elements (C. J. Hansen et al. 2014).

Two scenarios are still debated to explain the abundance pattern of CEMP-rs stars. The measured abundances in CEMP-rs stars could be produced by the intermediate neutron-capture process (*i*-process) occurring in low-to-intermediate mass asymptotic giant branch stars (J. J. Cowan &

Table 1
Atmospheric Parameters of the Program Stars

Name	$T_{\rm eff}$ (K)	log g (cm s^{-2})	ξ (km s^{-1})	[Fe/H]	Bin	Reference Stellar Parameters	Reference Literature Classification	Reference Binarity
CEMP-rs stars								
CS 22891−171	5215 ± 68	1.24 ± 0.09	2.14 ± 0.14	−2.50 ± 0.10	Y	(1)	(1)	(12, 15)
CS 22947-187	5200 ± 62	1.50 ± 0.12	1.70 ± 0.08	−2.55 ± 0.10	Y	(2)	(3)	(13, 14)
HD 145777	4443 ± 57	0.50 ± 0.10	2.63 ± 0.10	−2.32 ± 0.10	Y	(1)	(1)	(8)
HD 187861	5000 ± 100	1.50 ± 0.25	2.00 ± 0.20	−2.60 ± 0.10	Y	(1)	(1)	(11)
HD 196944	5168 ± 48	1.28 ± 0.16	1.68 ± 0.11	−2.50 ± 0.09	Y	(1)	(1)	(1)
HD 224959	4969 ± 64	1.26 ± 0.29	1.63 ± 0.14	−2.36 ± 0.09	Y	(1)	(1)	(10)
SDSS J0912+0216	6140 ± 37	4.60 ± 0.21	1.19 ± 0.07	−2.83 ± 0.07	⋯	(2)	(4)	⋯
SDSS J1349−0229	6238 ± 95	4.41 ± 0.21	1.45 ± 0.08	−3.13 ± 0.07	Y	(2)	(4)	(4)
CEMP-s stars								
SDSS J1036+1212	5591 ± 99	3.70 ± 0.08	0.87 ± 0.10	−3.48 ± 0.09	Y	(2)	(4)	(16, 17)
CS 22887−048	6500 ± 50	3.20 ± 0.15	1.00 ± 0.05	−2.10 ± 0.09	Y	(1)	(1)	(12, 13)
CS 22942−019	5100 ± 98	2.19 ± 0.20	1.73 ± 0.10	−2.50 ± 0.09	Y	(1)	(1)	(6, 7)
CS 29512−073	5471 ± 82	2.78 ± 0.16	1.28 ± 0.08	−2.35 ± 0.09	Y	(2)	(5)	(12, 13)
CS 30322−023	4500 ± 100	1.00 ± 0.50	2.80 ± 0.10	−3.35 ± 0.09	⋯	(1)	(1)	⋯
HD 26	5169 ± 108	2.46 ± 0.18	1.46 ± 0.08	−0.98 ± 0.09	Y	(1)	(1)	(8)
HD 55496	4642 ± 39	1.65 ± 0.14	1.33 ± 0.08	−2.10 ± 0.09	Y	(1)	(1)	(7, 9)
HD 198269	4458 ± 15	0.83 ± 0.08	1.64 ± 0.09	−2.10 ± 0.10	Y	(1)	(1)	(10)
HD 206983	4200 ± 100	0.60 ± 0.20	1.50 ± 0.10	−1.00 ± 0.10	Y	(1)	(1)	(7)

Note. The effective temperature $T_{\rm eff}$, surface gravity log g, microturbulence ξ, and metallicity [Fe/H] are presented. The stars are grouped as CEMP-rs or CEMP-s stars according to their previous literature classification. The classification derived from the analysis of the present paper is listed in Table 4.
References: (1) K21; (2) this work; (3) A. McWilliam et al. (1995); (4) N. T. Behara et al. (2010); (5) I. U. Roederer et al. (2014); (6) G. W. Preston & C. Sneden (2001); (7) A. Jorissen et al. (2005); (8) A. Jorissen et al. (2016); (9) C. B. Pereira et al. (2019); (10) R. D. McClure & A. W. Woodsworth (1990); (11) Gaia Collaboration et al. (2023); (12) Gaia Collaboration (2022); (13) T. C. Beers et al. (2000); (14) S. Buder et al. (2021); (15) T. C. Beers et al. (1992); (16) P. Bonifacio et al. (2021); (17) C. P. Ahn et al. (2012).

W. K. Rose 1977; N. Iwamoto et al. 2004; M. Hampel et al. 2016, 2019; P. A. Denissenkov et al. 2017; P. Denissenkov et al. 2018; P. P. Goswami & A. Goswami 2020; A. Choplin et al. 2021, K21). Alternatively, CEMP-rs stars could also be the result of two independent pollutions, one by the *s*-process and another one by the *r*-process (K. Jonsell et al. 2006; M. Lugaro et al. 2009; S. Bisterzo et al. 2011; C. Abate et al. 2016). These scenarios seem to account for some objects, such as the one presented in M. Gull et al. (2018).

Though CEMP-rs stars are by definition enhanced in *r*-process elements, the overabundances are mostly measured from Eu, Gd, or Dy. This is mainly due to the difficulty of measuring heavy *r*-process elements using the optical spectra, as their most sensitive lines are in the UV. A major goal of this study is to determine whether heavy *r*-process elements are enhanced in CEMP-rs stars and to gain insights into their production mechanisms. Some of them were confirmed as CEMP-rs stars in our earlier study (K21), while others are taken from the literature (A. McWilliam et al. 1995; N. T. Behara et al. 2010). The study also includes a few CEMP-s stars for comparison. Although sites such as neutron star mergers are potentially identified as possible sources of *r*-process elements, their exact contribution to the galactic chemical evolution and to the solar abundances remains to be clarified. Hence, it is crucial to identify the possible source of these elements and the level of production at these sites.

The structure of the paper is as follows. The sample selection of CEMP-s and CEMP-rs stars is outlined in Section 2, followed in Section 3 by the derivation of the stellar parameters and abundances. Individual lines are discussed in Section 4. Section 5 presents the classification of stars using different diagnostic indicators. Section 6 presents a comparison with nucleosynthesis predictions, while Section 7 provides a discussion on the classification scheme. Section 8 focuses on the comparison of heavy *r*-process abundances in different CEMP classes. Finally, Section 9 lists the discussions and conclusions of this paper.

2. Sample Selection

Our stellar sample consists of 17 stars as listed in Table 1 among which 12 stars are previously analyzed in K21, for which we derive or, in some cases, update (using improved line selection) the abundances of Gd, Tb, Dy, Ho, Er, Tm, Yb, Lu, Hf, Ta, Os, and Ir. For several of these elements, particularly Tb, Ho, Tm, Yb, Lu, Ta, Os, and Ir, the abundances were not derived in K21 and are presented here for the first time. New UVES VLT spectra have been obtained (ESO proposals 105.20LJ.001 and 105.20LJ.002) for five objects of K21. Additionally, we used the UVES archival spectra for five new objects; they are listed along with atmospheric parameters from the previous studies, in Table 2.

The approximate resolution is $R = \lambda/\Delta\lambda = 47{,}000$ and the spectral coverage is from 3280 to 6835 Å.

The sample thus consists of eight CEMP-rs stars and nine CEMP-s stars, according to previous literature classification, as referenced in Table 1. Following the analysis in the present paper, this classification will in some instances be changed (see Section 5).

Concerning binarity, as listed in Table 1, most of the stars are confirmed binaries. Only CS 30322−023 and SDSS J0912 +0216 lack binarity confirmation.

Table 2
A Comparison of the Stellar Parameters of the Program Stars with Literature

Name	$T_{\rm eff}$ (K)	log g (cm s^{-2})	[Fe/H]	References
CS 22947−187	5200 ± 62	1.50 ± 0.12	−2.55 ± 0.10	(1)
	5160	1.30 ± 0.25	−2.49	(2)
	5300 ± 52	1.40 ± 0.37	−2.58 ± 0.06	(3)
SDSS	6140 ± 37	4.60 ± 0.21	−2.83 ± 0.07	(1)
J0912+0216	6500	4.5	−2.50	(4)
	6150	4.0	−2.68	(5)
SDSS	5591 ± 99	3.70 ± 0.08	−3.48 ± 0.09	(1)
J1036t+1212	6000	4.0	−3.20	(4)
	5850	4.0	−3.47	(5)
SDSS	6238 ± 95	4.41 ± 0.21	−3.13 ± 0.07	(1)
J1349−0229	6200	4.0	−3.00	(4)
	6200	4.0	−3.40	(5)
CS 29512−073	5471 ± 82	2.78 ± 0.16	−2.35 ± 0.09	(1)
	5650 ± 52	3.60 ± 0.23	−1.93 ± 0.07	(3)
	5852	2.88	−2.15	(6)

Note. The stellar parameters (effective temperature, surface gravity, and metallicity) for the program stars that were not discussed in K21 are compared with literature values.
References. (1) This work; (2) A. McWilliam et al. (1995); (3) I. U. Roederer et al. (2014); (4) N. T. Behara et al. (2010); (5) W. Aoki et al. (2013); (6) G. Limberg et al. (2021).

3. Derivation of the Atmospheric Parameters and Elemental Abundances

The atmospheric parameters, $T_{\rm eff}$, log g, ξ, and [Fe/H] are derived using the BACCHUS code (T. Masseron et al. 2016) in a semiautomated mode as explained by D. Karinkuzhi et al. (2018, 2021) and are listed in Table 1. As can be seen in Table 2, the agreement between the stellar parameters derived in the present work and those of previous studies is reasonable. The objects already discussed in K21 are not further mentioned here.

The abundances are derived by comparing the observed spectra with synthetic ones produced by the 1D local thermodynamic equilibrium (LTE) TURBOSPECTRUM radiative transfer code (R. Alvarez & B. Plez 1998) using MARCS model atmospheres (B. Gustafsson et al. 2008). The M. Asplund et al. (2009) solar abundances were adopted. Individual elemental abundances were calculated using line lists from U. Heiter et al. (2015; 2021). The atomic lines used to derive the abundances of all the elements are presented in Table A1. The abundances were derived under LTE conditions, but non-LTE (NLTE) corrections were applied when they were available in the literature for stars of similar stellar parameters. Only the abundances of the heavy r elements are listed in Table B2 for the stars already analyzed by K21. However, the full list of derived abundances is presented for the five objects not included in K21.

4. Comments on Individual Abundances

We present the atomic and molecular lines used to derive the elemental abundances for the five objects that were not in K21. For the remaining objects, we only discuss the heavy *r*-process elements. Lithium could be a sensitive diagnostic of the *i*-process, since it is known to be produced during proton ingestion events (e.g., N. Iwamoto et al. 2004; S. Cristallo et al. 2009; A. Choplin et al. 2024b), at least if not destroyed during subsequent AGB evolutionary phases. Unfortunately it could not be measured in any of our targets.

4.1. C, N, and O in the Five New Objects

The carbon (C) abundance is derived using only the CH *G* band at 4310 Å because the C_2 bands are very weak due to their rather high temperatures. The oxygen abundance is measured using the forbidden line at 6300.303 Å. We could derive the nitrogen abundance in all five objects using the CN bands at 3883 Å.

The $^{12}C/^{13}C$ ratio is determined using ^{12}CH and ^{13}CH features in the *G*-band region near 4300 Å (Figure 1). The ^{12}CN and ^{13}CN features around 3883 Å were also used for confirmation (Figure 2). The differences between the $^{12}C/^{13}C$ ratios estimated from the *G* band and the 3883 Å region are very small (of the order of ±3.0 units for all objects) except for CS 29512−073, where we find $^{12}C/^{13}C = 19$ when derived from the CH band and 11.5 from the CN band.

4.2. Light Elements: Na, Mg, Ca, Sc, Ti, Cr, Mn, Co, Ni, Cu, and Zn

The abundances of the light elements are derived using the lines listed in Table A.1 of K21. For the five new objects, the derived abundances are presented in Table B1, while for the others, they are listed in Table B.1 of K21. We could not measure the Na abundance in SDSS J1349−0229 because the Na lines were too strong and saturated. The Mg abundance was derived exclusively from the Mg I line at 5528.405 Å. However, for the other two objects, both the Mg I line at 5528.405 and 5711.088 Å were used to derive the Mg abundance. S. Alexeeva et al. (2018) calculated an NLTE correction of 0.02 dex for the 5528.405 Å Mg I line, corresponding to the following atmospheric parameters: $T_{\rm eff} = 6350$ K, log $g = 4.09$, and [Fe/H] $= -2.08$. The stellar parameters of the stars in S. Alexeeva et al. (2018) are close but do not exactly match those of our objects; therefore, no NLTE correction was applied to our Mg abundances. However, from S. Alexeeva et al. (2018) we infer that the NLTE corrections for the Mg I lines at 5528.405 and 5711.088 Å would probably be very small. The α-elements show an average enrichment with [X/Fe] = 0.56, considering all the stars in our sample.

The lines that were used for the abundance determination of light elements in addition to those listed in Table A.1 of K21, are listed in Table A1.

4.3. S-Process Elements: Sr, Y, Zr, Nb, Mo, Ba, La, Ce, Pr, and Nd

The abundances are listed in Table B1, some specific comments can be found below.

Strontium. The Sr abundance is derived in the five new stars using Sr II lines at 3464.453, 4077.707, and 4215.520 Å . In K21, Sr I lines at 4607.327, and 7070.070 Å were also used, which are either absent or blended in these spectra, hence were not used in this analysis. The NLTE corrections were taken from M. Bergemann et al. (2012) and L. Mashonkina et al. (2008, 2023) and, for the parameter range of all objects, they are minor, ranging from 0.01 to −0.03 dex. The only exception is SDSS J1036+1212, for which an NLTE correction of 0.14 dex for the 4077.707 Å Sr II line was applied, corresponding to a star with the following stellar parameters ($T_{\rm eff} = 5600$ K, log $g = 3.80$, and [Fe/H] $= -3.48$) taken from M. Bergemann et al. (2012).

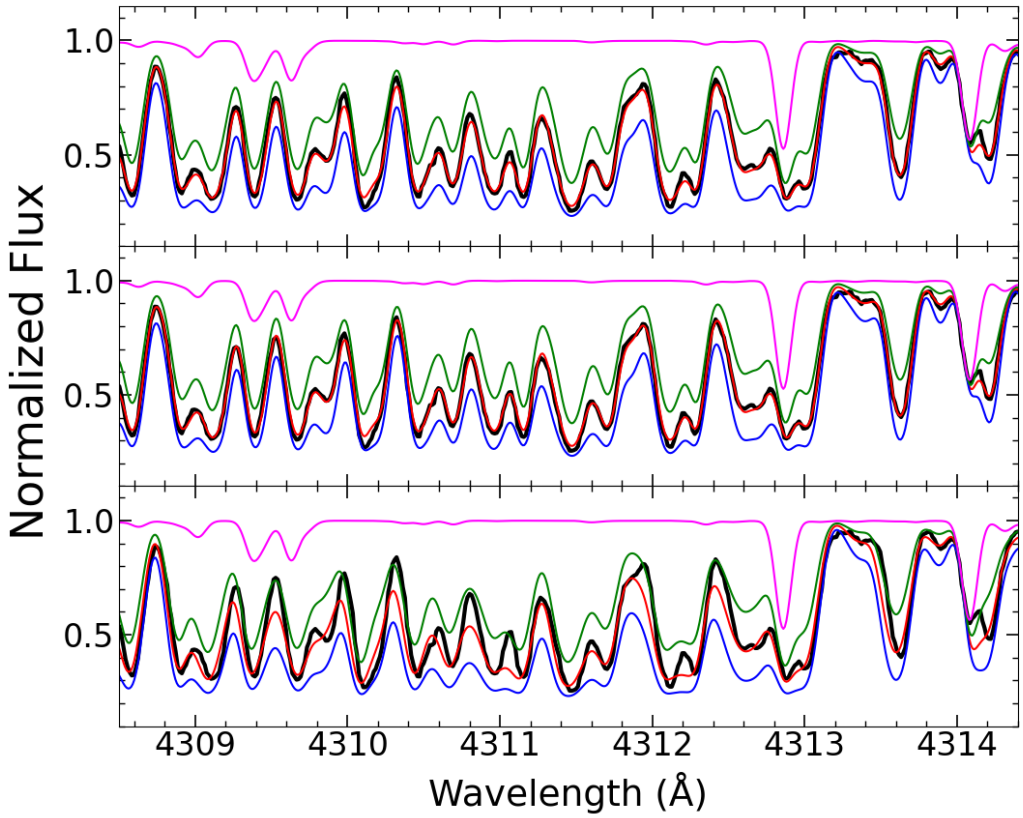

Figure 1. Spectral fits for the determination of $^{12}C/^{13}C$ ratio using the CH *G* band at 4310 Å in CS 29512−073. The upper (respectively, middle and bottom) panel shows spectral synthesis with $^{12}C/^{13}C = 30$ (respectively, 19 and 1.5). The red curve depicts the synthetic spectrum for an abundance of log ϵ (C) = 7.45, with the blue and green curves illustrating ±0.3 dex variations. The black line represents the observed spectrum, and the magenta line corresponds to the spectral synthesis without carbon.

Yttrium. Many unblended or clean lines are available to measure the Y abundances. For CS 22947−187 and CS 29512 −073, an NLTE correction of 0.12 dex is adopted, corresponding to the average NLTE correction (for the lines that we used) computed in S. Alexeeva et al. (2023) for HD 122563 ($T_{\rm eff}$ = 4600 K, log g = 1.43, and [Fe/H] = −2.55).

For SDSS J1036+1212, we applied corrections of 0.06 dex (respectively, 0.07 dex), for the Y II 4883.684 Å (respectively, 4900.120 Å) lines, since these values were computed by S. Alexeeva et al. (2023) for HD 140283, which has closely matching stellar parameters ($T_{\rm eff}$ = 5780 K, log g = 3.7, and [Fe/H] = −2.46).

In the same vein, since SDSS J0912+0216 and SDSS J1349 −0229 have stellar parameters similar to those of HD 84937 ($T_{\rm eff}$ = 6350 K, log g = 4.09, and [Fe/H] = −2.12), a turn-off very metal-poor star analyzed by S. Alexeeva et al. (2023), we used their NLTE corrections of 0.06 dex for Y II lines at 4883.684 and 4900.120 Å.

We note that all our LTE abundances seem to be underestimated when compared to the model predictions (see Section 6), and that NLTE corrections tend to reduce this discrepancy, since S. Alexeeva et al. (2023) measured positive NLTE corrections for all these lines with an average value of 0.21 dex for the parameter range corresponding to HD 122563.

Zirconium. In addition to the Zr II lines listed in K21, we also used the Zr II lines at 4208.977 and 4359.720 Å.

Niobium. The Nb II lines at 3425.425 and 3426.531 Å were used to derive Nb abundance in CS 29512−073 and SDSS J1349−0229. For SDSS J1036+1212, the Nb II lines at 3651.187 Å were used to estimate the Nb abundance. Niobium (Nb) could be reliably measured only in these three stars among the five new objects analyzed in this study.

Molybdenum. The Mo abundance is measured in all the program stars using the line at 3864.103 Å as this is the only line available that is sensitive enough for abundance determination in our wavelength range.

Barium. The Ba II lines at 5853.673, 6141.711, and 6496.895 Å were used to derive Ba abundance in SDSS J1349 −0229 and SDSS J0912+0216. For the other three objects, we could also use the Ba II line at 4166.000 Å.

Lanthanum. The La II lines at 4920 and 4921 Å, for which HF splitting is available, are primarily used to estimate the La abundance.

The lines used to derive the abundances of Ce, Pr, and Nd are presented in the Table A1.

4.4. r-process Elements: Sm, Eu, Gd, Tb, Dy, Ho, Er, Tm, Yb, Lu, Hf, Ta, Os, and Ir

In K21, the abundances of Sm, Eu, Gd, Dy, Er, Hf, and Os were determined for most stars. Abundances of Tb, Ho, Tm, and Yb for the five stars from K21 have been reported in our previous work (M. Riyas et al. 2024). In the present paper, we could add abundance determinations for five new objects and also complement these abundances with those of the heavy *r*-elements Tb, Ho, Tm, Yb, Lu, Ir, and Ta. A few fits are illustrated on Figure 3.

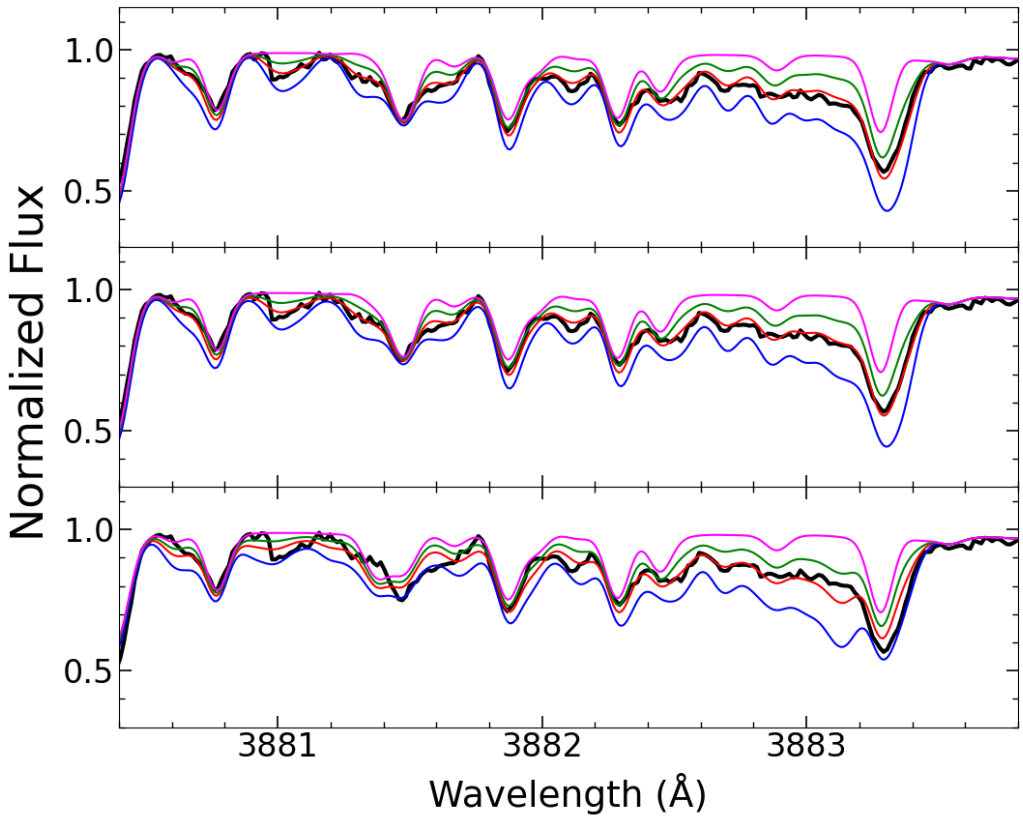

Figure 2. Spectral fits for determining the $^{12}C/^{13}C$ ratio using the CN band at 3883 Å in CS 29512−073. The upper (respectively, middle and bottom) panel shows spectral synthesis with $^{12}C/^{13}C = 30$ (respectively, 11.5 and 1.5). The red curve depicts the synthetic spectrum for an abundance of $\log \epsilon(N) = 6.10$, with the blue and green curves indicating the synthesis with ±0.3 dex variations. The black line represents the observed spectrum, and the magenta line corresponds to the spectral synthesis without nitrogen.

Samarium. The Sm II lines at 4318.926, 4390.854, and 4420.520 Å were used to derive the Sm abundance for SDSS J0912+0216 and SDSS J1349−0229, while the line at 3941.876 Å was used for SDSS J1036+1212. For CS 22947−187 and CS 29512−073, many Sm lines were accessible between 4000 and 5000 Å as listed in Table A1 of Appendix A.

Europium. We determined the LTE and NLTE Eu abundances independently, as detailed in Section 4.6 of K21, and the results are shown in Table B1.

L. Mashonkina et al. (2008) calculated the NLTE correction of 0.16 dex for the Eu II line at 4129.680 Å in HD 122563 ($T_{\rm eff}$ = 4600 K, $\log g$ = 1.50, [Fe/H] = −2.53). The Eu abundance is derived using the same line for CS 22947−187 and CS 29512−073, so the same NLTE correction is applied to get the final Eu abundance since their parameters are similar to those of HD 122563. The Eu_{LTE} in Table B1 is the average Eu abundance calculated without the 4129.680 Å line. The Eu abundance for SDSS J1349−0229 is obtained using the Eu II line at 4205.065 Å. We applied the NLTE correction of 0.11 dex from L. Mashonkina & N. Christlieb (2014), corresponding to the closest parameters $T_{\rm eff}$ = 5260 K, $\log g$ = 2.75, [Fe/H] = −2.85. As these stellar parameters are different from the ones of SDSS J1349-0229, we list in Table B1 both the LTE and the (uncertain) non-LTE abundance.

For SDSSJ 1036+1212, we used the two Eu II lines at 3907.108 and 3930.506 Å to derive the Eu abundance. L. Mashonkina & N. Christlieb (2014) listed the NLTE corrections of 0.04 and 0.05 dex, respectively, for the 3907.108 and 3930.506 Å lines, corresponding to the parameters $T_{\rm eff}$ = 5010 K, $\log g$ = 4.80, and [Fe/H] = −3.40, which are close to those of SDSSJ 1036+1212.

We calculated the Eu abundance for SDSSJ 0912+0216 using the three Eu II lines at 3819.684, 3907.108, and 4205.065 Å. L. Mashonkina & N. Christlieb (2014) reported the NLTE corrections of 0.12, 0.15, and 0.11 dex, respectively, for these three lines, corresponding to the parameters $T_{\rm eff}$ = 5260 K, $\log g$ = 2.75, [Fe/H] = −2.85, which are similar to those of SDSSJ 0912+0216.

Gadolinium. Gd II lines at 3545.790 and 3768.396 Å are used in addition to the Gd II line at 4251.731 Å used by K21 for deriving the Gd abundance in SDSS J0912+0216 and SDSS J1036+1212.

Terbium. A single Tb II line at 3939.539 Å is used to compute the Tb abundance in HD 145777. For HD 26, we used only the 3658.888 Å line (leading to $\log \epsilon$ = 0.90 dex), since the 3625.510 Å line (leading to $\log \epsilon$ = 0.30 dex) appears to be affected by an unidentified feature.

Dysprosium. For HD 206983, Dy abundance is measured using the Dy II line at 4103.306 Å line, which is strong (20% of the local continuum) and blended by a Fe I line at 4103.298 Å. For HD 26, this Dy line at 4103.306 Å is also strong (40% of the local continuum), and it is marked as uncertain in Table B2.

Holmium. The Ho II line at 3810.738 Å could be used in CS 29512–073 and HD 196944, in addition to the other Ho lines as listed in Appendix A.

Thulium. A total of seven Tm II lines are used for deriving the Tm abundance in the program stars. The spectral synthesis

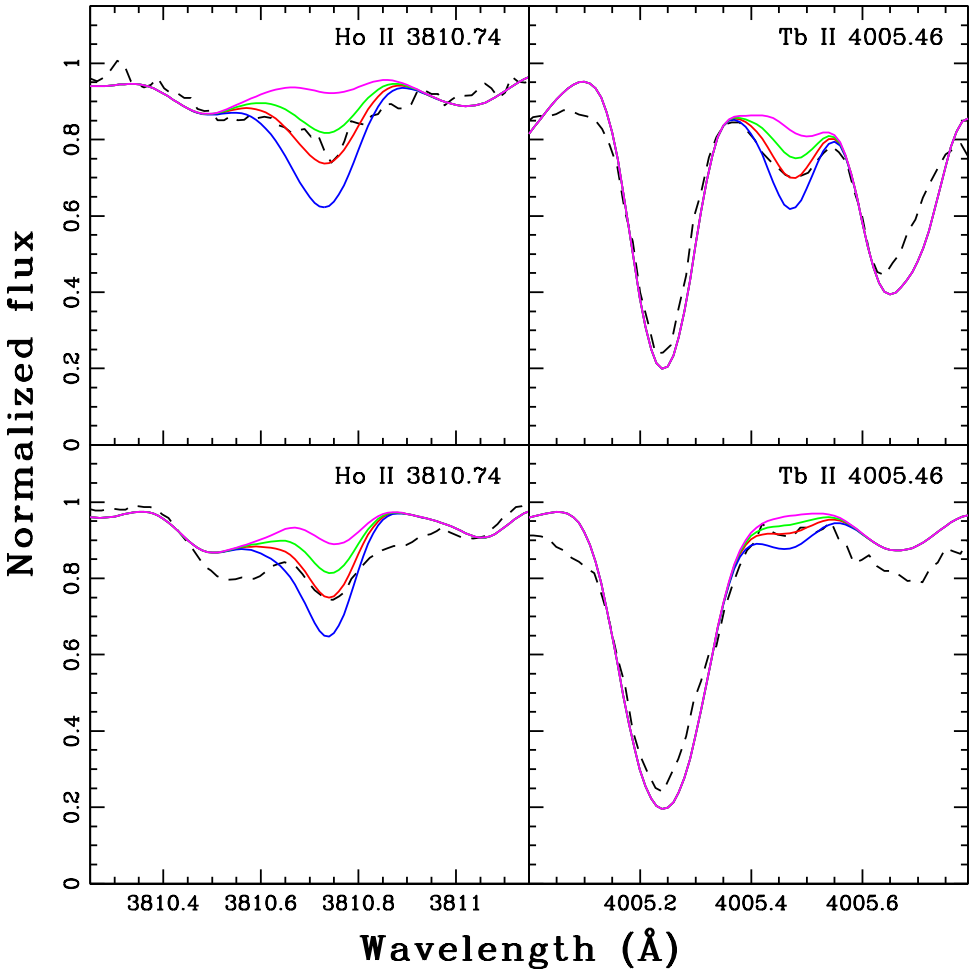

Figure 3. The upper and lower left panels display the spectral fitting of the Ho II lines for CS 22947−187 and HD 196944, while the upper and lower right panels display the Tb II lines for HD 224959 and CS 30322−023. Red lines correspond to spectral syntheses with the adopted Ho II abundances of −1.6 dex, −2.0 dex for CS 22947−187 and HD 196944, and Tb II abundances of −0.75 dex, −2.0 dex for HD 224959 and CS 30322−023, respectively. Blue and green lines correspond to syntheses with abundances deviating by ±0.3 dex from the adopted abundance. The black dashed line represents the observed spectrum. The magenta line corresponds to the synthesis with a null abundance for the corresponding element.

of the 3795.76 Å Tm line is presented in Figure 4. The Tm II lines at 3700.255 and 3701.362 Å are used in all our program stars, but in HD 198269, the Tm II line at 3700.255 Å is slightly blended on the right wing. Although the abundance from this line is consistent with the one from the line at 3701.362 Å it is not included in the analysis.

Ytterbium. The Yb abundance is measured in all the program stars using the Yb II line at 3694.192 Å (Figure 4), as it is the only line sufficiently sensitive that we could identify for abundance determination. However, in some stars (HD 26, HD 198269, HD 206983, and HD 224959) it is very strong ($\leqslant$30% of the local continuum), and therefore rejected, because the core of the line must form in the upper layers of the photosphere, where the LTE approximation vanishes.

Lutetium. In HD 198269, the Lu II line at 3507.395 Å, which is measurable in most other stars, is absent. Therefore, the Lu abundance is determined using the other two Lu II lines: 5983.701 and 6221.592 Å, leading to $\log \epsilon = -0.10$ dex and −0.80 dex, respectively. Given the discrepancy between these two values, the Lu abundance (computed as their average) is considered highly uncertain.

Hafnium. The Hf II lines at 3918.090 and 4093.150 Å yield consistent abundances in all the stars where they are detectable. When they could not be measured, we used the other Hf lines listed in Appendix A.

Tantalum. Eight lines of Ta II could be identified in the spectra, as listed in Table A1. Two lines are illustrated on Figure 5. However, because of a poor agreement between synthetic and observed spectra, only upper limits or uncertain abundances could be derived for all the stars except for HD 196944. For HD 196944, the best fit was obtained from the 3414.128 Å line ($\log \epsilon = -0.60$ dex), providing an abundance roughly in agreement with the (clearly less well-fitted) 3057.232 and 3056.603 Å lines ($\log \epsilon \sim -0.40$ dex), but in conflict with the 3440.312 Å line ($\log \epsilon = 0.30$ dex). Table B2 lists the Ta abundance of HD 196944 derived from the sole 3414.128 Å line.

Osmium. We investigated three Os lines: 4135.781, 4260.849, and 4420.477 Å. It turns out that the 4135.781 Å line gives higher abundance (by 0.60 dex) than the 4260.849 and 4420.477 Å lines in HD 55496 and CS 22891−171. In addition, the abundance derived from the 4135.781 Å line is much larger than the model predictions. Therefore, this line

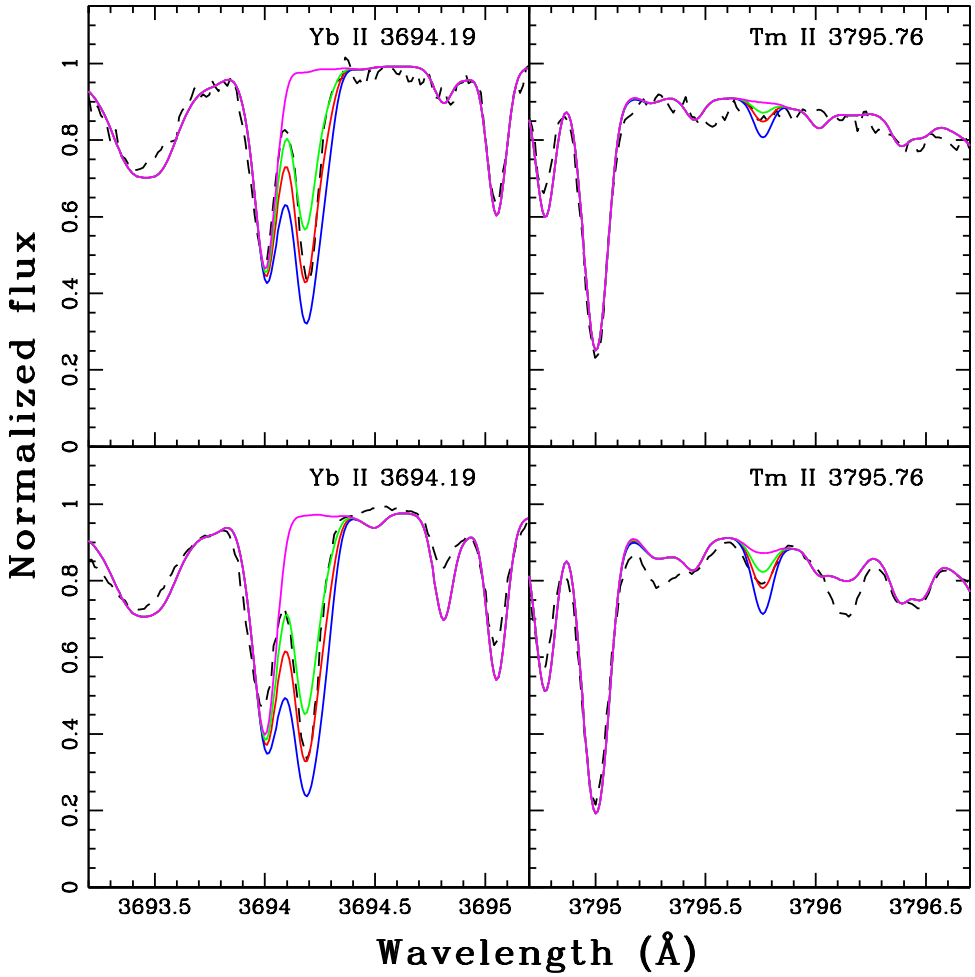

Figure 4. Spectral fitting of the Yb II and Tm II lines is shown for two CEMP stars, CS 29512–073 and HD 196944, in the upper and lower panels, respectively. Red lines correspond to spectral syntheses with the adopted Yb II, Tm II abundances of −0.55 dex, −1.20 dex for CS 29512–073, and −1.05 dex, −1.60 dex for HD 196944, respectively. The blue, green, magenta, and black curves have the same meaning as in Figure 3.

was rejected, and the Os abundance (or upper limit) as listed in Table B2 was only derived from the 4260.849 and 4420.477 Å lines.

Iridium. The Ir I line at 3992.121 Å is sensitive, but the overall agreement in this spectral region is not satisfactory. Some additional Ir lines are sometimes visible, but we only provide upper limits or uncertain Ir abundances in Tables B1 and B2.

4.5. The Third Peak s-process Element Pb

The Pb I line at 4057.807 Å is the only suitable one to measure the Pb abundance in our spectra. The hyperfine splitting is taken into account. NLTE corrections of +0.37, +0.62, and +0.52 dex were adopted for CS 22947−187, CS 29512−073, and SDSS J1349−0229, respectively, based on the values derived by L. Mashonkina et al. (2012) for stars with comparable stellar parameters.

4.6. Uncertainties in Abundances

The uncertainties on the elemental abundances were obtained from Equation (2) of J. A. Johnson (2002), following the procedure explained in D. Karinkuzhi et al. (2018, K21):

$$\begin{aligned}\sigma_{\rm tot}^2 = \sigma_{\rm ran}^2 &+ \left(\frac{\partial \log \epsilon}{\partial T}\right)^2 \sigma_T^2 \\ &+ \left(\frac{\partial \log \epsilon}{\partial \log g}\right)^2 \sigma_{\log g}^2 + \left(\frac{\partial \log \epsilon}{\partial \xi}\right)^2 \sigma_\xi^2 \\ &+ \left(\frac{\partial \log \epsilon}{\partial [{\rm Fe/H}]}\right)^2 \sigma_{\rm [Fe/H]}^2 \\ &+ 2\left[\left(\frac{\partial \log \epsilon}{\partial T}\right)\left(\frac{\partial \log \epsilon}{\partial \log g}\right)\sigma_{T\,\log g}\right. \\ &+ \left(\frac{\partial \log \epsilon}{\partial \xi}\right)\left(\frac{\partial \log \epsilon}{\partial \log g}\right)\sigma_{\log g \xi} \\ &+ \left.\left(\frac{\partial \log \epsilon}{\partial \xi}\right)\left(\frac{\partial \log \epsilon}{\partial T}\right)\sigma_{\xi T}\right]. \end{aligned} \quad (1)$$

In Equation (1), $\log \epsilon$ represents an elemental abundance, while σ_T, $\sigma_{\log g}$, and σ_ξ are the typical uncertainties on the atmospheric parameters, which are estimated to be $\sigma_T = 75$ K, $\sigma_{\log g} = 0.2$ dex, $\sigma_\xi = 0.05$ km s^{-1}, and $\sigma_{\rm [Fe/H]} = 0.10$ dex. The partial derivatives appearing in Equation (1) were

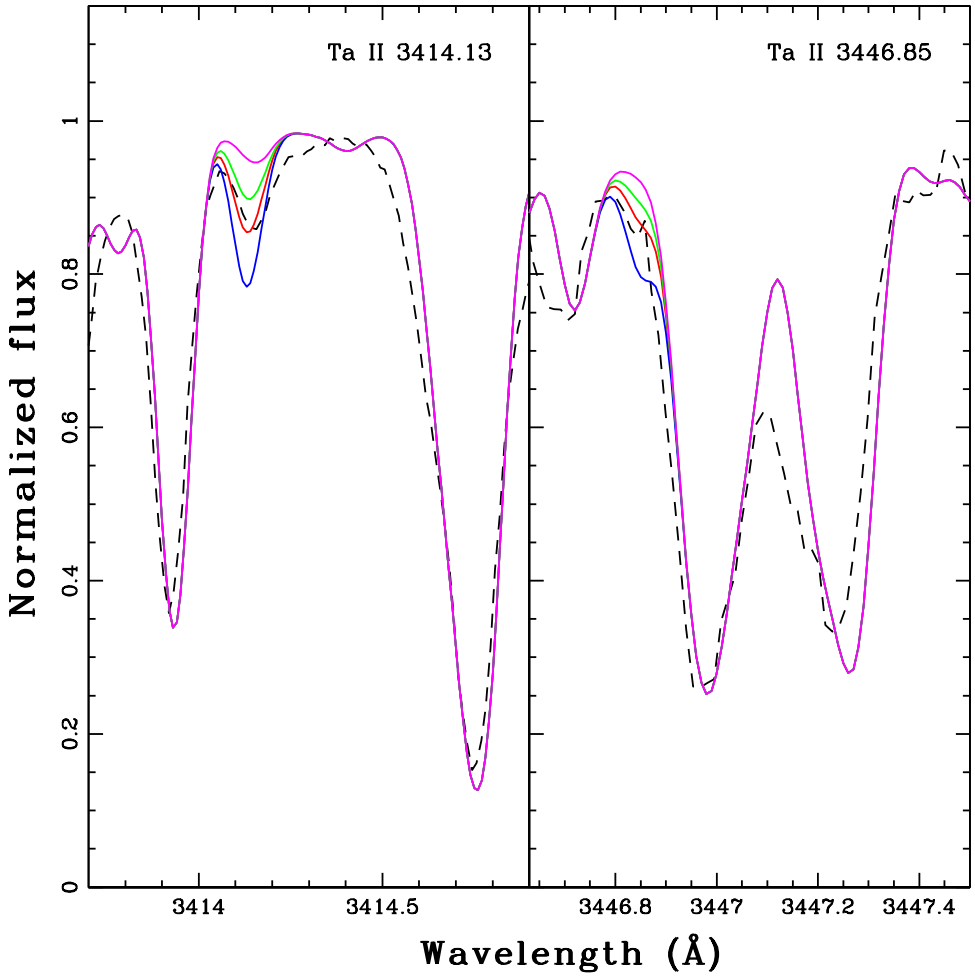

Figure 5. The spectral fits for the Ta II lines at 3414.13 and 3446.85 Å are presented for HD 196944 in the left and for HD 224959 in the right panels, respectively. The red curve represents the synthesis with the adopted abundances (−0.6 dex for the left panel and −0.25 dex for the right panel). The blue, green, magenta, and black curves have the same meaning as in Figure 3.

determined in the particular cases of CS 22947-187 and HD 224959, varying the atmospheric parameters $T_{\rm eff}$, $\log g$, microturbulence ξ, and [Fe/H] by 100 K, 0.5, 0.5 km s^{-1}, and 0.5 dex, respectively, and the corresponding abundance changes are provided in Table 3. We adopt the covariances $\sigma_{T\log g} = -0.5$, $\sigma_{\log g\xi} = 0.02$, and $\sigma_{\xi T} = 3$, as measured by K21, since these cases are specifically found for HD 196944 and HD 198269. Similarly, here the objects, CS 22947−187 and HD 224959, also exhibit stellar parameters that are almost comparable to those of HD 196944 and HD 198269.

We assumed a random error $\sigma_{\rm ran} = 0.1$ dex if only one line is used to derive the abundance. Otherwise we have calculated $\sigma_{\rm ran}$ as $\sigma_{\rm ran} = \sigma_l/N^{1/2}$, where σ_l is the standard deviation of the abundances derived from the N lines of the considered element. The final uncertainties are then calculated using Equation (2) and are presented in Tables B1 and B2. The final error in abundance ratios ($\sigma_{\rm [X,Fe]}$) is calculated using Equation (6) of J. A. Johnson (2002).

$$\sigma^2_{\rm [X/Fe]} = \sigma^2_{\rm X} + \sigma^2_{\rm Fe} - 2\,\sigma_{\rm X,Fe}, \tag{2}$$

where $\sigma_{\rm X,Fe}$ is the covariance between two abundances (X and Fe), and is given by:

$$\begin{aligned}\sigma_{\rm X,Fe} = &\left(\frac{\partial \log \epsilon_X}{\partial T}\right)\left(\frac{\partial \log \epsilon_{Fe}}{\partial T}\right)\sigma^2_T \\ &+ \left(\frac{\partial \log \epsilon_X}{\partial \log g}\right)\left(\frac{\partial \log \epsilon_{Fe}}{\partial \log g}\right)\sigma^2_{\log g} \\ &+ \left(\frac{\partial \log \epsilon_X}{\partial \xi}\right)\left(\frac{\partial \log \epsilon_{Fe}}{\partial \xi}\right)\sigma^2_\xi \\ &+ \left[\left(\frac{\partial \log \epsilon_X}{\partial T}\right)\left(\frac{\partial \log \epsilon_{Fe}}{\partial \log g}\right)\right. \\ &\left.+ \left(\frac{\partial \log \epsilon_X}{\partial \log g}\right)\left(\frac{\partial \log \epsilon_{Fe}}{\partial T}\right)\right]\sigma_{T\log g} \\ &+ \left[\left(\frac{\partial \log \epsilon_X}{\partial \xi}\right)\left(\frac{\partial \log \epsilon_{Fe}}{\partial \log g}\right)\right. \\ &\left.+ \left(\frac{\partial \log \epsilon_X}{\partial \log g}\right)\left(\frac{\partial \log \epsilon_{Fe}}{\partial \xi}\right)\right]\sigma_{\xi\log g}.\end{aligned} \tag{3}$$

Table 3
Uncertainties in Abundances

Element	$\Delta \log \epsilon_X$			
	$\Delta T_{\rm eff}$ (+100 K)	$\Delta \log g$ (+0.5)	$\Delta \xi_t$ (+0.5 km s^{-1})	Δ [Fe/H] (+0.5 dex)
C	0.20	−0.15	−0.05	0.00
N	0.15	0.05	0.10	0.00
O	0.10	0.20	0.05	0.05
Na	0.05	0.00	0.00	0.00
Mg	0.05	0.00	−0.05	0.00
Ca	0.06	−0.03	−0.09	−0.01
Sc	0.05	0.18	−0.02	0.00
Ti	0.09	0.10	0.00	0.06
Cr	0.08	0.00	−0.06	−0.06
Mn	0.10	0.00	0.00	0.00
Fe	0.14	0.06	−0.10	0.01
Co	0.13	0.00	−0.10	0.00
Ni	0.08	0.00	−0.02	0.01
Cu	0.10	−0.05	0.00	0.00
Zn	0.05	0.05	−0.05	0.00
Sr	0.13	0.20	−0.47	−0.05
Y	0.05	0.16	0.00	0.01
Zr	0.00	0.05	0.00	0.00
Mo	0.05	−0.10	−0.10	0.00
Ba	0.03	0.18	−0.13	0.02
La	0.07	0.15	0.00	0.02
Ce	0.05	0.15	0.00	0.02
Pr	0.05	0.10	0.00	0.02
Nd	0.05	0.15	−0.03	0.02
Sm	0.07	0.14	−0.02	0.02
Eu	0.03	0.10	−0.02	−0.02
Gd	0.07	0.17	0.00	0.02
Tb	0.10	0.15	−0.03	0.03
Dy	−0.05	0.05	−0.08	0.00
Ho	0.05	0.12	0.00	0.00
Er	0.08	0.22	−0.02	0.02
Tm	0.00	0.13	0.02	0.03
Yb	0.05	0.15	−0.10	0.00
Lu	0.06	0.22	0.00	0.02
Hf	0.07	0.22	0.00	0.05
Ta	0.07	−0.03	−0.11	0.02
Os	0.15	0.05	0.00	0.00
Ir	0.06	0.10	0.00	0.00
Pb	0.10	0.00	0.00	0.00

Note. Abundance variations ($\Delta \log \epsilon_X$) with variations of the atmospheric parameters in CS 22947−187. The terbium and osmium lines are extremely close to the continuum in CS 22947−187; we thus used a star with similar stellar parameters, HD 224959 (see Table 1) to estimate the abundance sensitivity to parameter changes for Tb and Os.

5. Classification

Distinguishing between CEMP-s and CEMP-rs stars is challenging and may even be unrealistic, particularly if CEMP-rs stars originate from an *i*-process capable of producing a wide range of abundance profiles, from s-type to rs-type. However, we describe various indicators below and discuss their consistency, as well as cases where they yield ambiguous results.

5.1. The [La/Eu] Indicator

In Table 4, the Class$_{sr}$ column is based on the [La/Eu] (or [Ba/Eu]) abundance ratio. With *X* standing for La or Ba, stars with [X/Eu] > 0.5 are categorized as CEMP-s, those with $0.0 \leqslant$ [X/Eu] $\leqslant 0.5$ as CEMP-rs, and those with [X/Eu] clearly negative as CEMP-r. Difficulties arise because the Ba and La diagnostics are sometimes conflicting (e.g., CS 22891 −171). HD 196944, with [La/Eu] = −0.01 but [Ba/Eu] = 0.24, is too close to the borderline to be considered as a CEMP-r star and is classified as CEMP-rs. Such indicators are prone to errors because they are based on a small number of elemental abundances, sometimes only on two line measurements. In the following, indicators based on a larger number of lines and elements are considered.

5.2. The "Distance" Indicator

In an attempt to establish a model-independent classification, we compute the "distance" of the measured abundance distribution to the canonical solar system *r*-process distribution. Although the *r*-process is not strictly universal, it is found to exhibit less variability (e.g., with metallicity) than the *s*-process and therefore serves as a more reliable reference point for quantifying abundance anomalies. The d_s and $d_{\rm rms}$ distances are detailed in Section 5 of K21 and are calculated using the element set: Y, Zr, Ba, La, Ce, Nd, Sm, and Eu. The limit between CEMP-s and CEMP-rs stars is, somewhat arbitrarily, placed at $d_s = 0.6$ ($d_{\rm rms} = 0.7$) to give consistent results. The classification based on both distance indicators is listed in columns Class$_{d_s}$ and Class$_{d_{\rm rms}}$ in Table 4.

5.3. The $^{12}C/^{13}C$ Ratio

In *s*-process AGB models (i.e., without proton ingestion episodes (PIE)), a surface $^{12}C/^{13}C$ ratio larger than typically 20–30 is found during the AGB phase (e.g., Figures 1 and 2 in A. Choplin et al. 2024a). Following a PIE, this ratio is predicted to range between 3 and 9 (N. Iwamoto et al. 2004; A. Choplin et al. 2024b) with a potential increase up to around 20 if additional thermal pulses occur.

The nine program stars classified as rs (last column of Table 4) have[5] $2.3 < {}^{12}C/^{13}C < 16$, with an average of 8.3. The two stars with an unclear classification (s or rs) have $^{12}C/^{13}C = 12$ and 24. Finally, the six stars classified as s have $5 < {}^{12}C/^{13}C < 16$, with a mean of 11.6. The low ratios found in rs stars are consistent with *i*-process model predictions. Also, on average, rs-stars exhibit lower $^{12}C/^{13}C$ ratios than s-stars, consistent with the lower values predicted by *i*-process models. Nevertheless, the ratios measured in s-stars are relatively low compared to those expected from *s*-process AGB models. However, the companion star that accreted material from the AGB donor may have subsequently undergone the first dredge-up, a process known to decrease the $^{12}C/^{13}C$ ratio (e.g., C. Charbonnel 1994). Among our program stars, 13 out of 17 have $\log g < 3$, suggesting they may have experienced the first dredge-up. Due to the possible surface effects related to the first dredge-up, we do not consider here the measured $^{12}C/^{13}C$ ratios as a robust indicator for distinguishing s from rs stars in our sample.

6. Comparison with Nucleosynthesis Predictions

6.1. AGB Models and Fitting Procedure

The enrichment in heavy elements measured in CEMP-s stars is thought to originate from a now-extinct AGB

[5] We considered the $^{12}C/^{13}C$ ratios derived from the CN band.

Table 4
Classification Based on s- and r-elements

Object	[s/r]			Distance				χ^2			Final Class
	[La/Eu]	[Ba/Eu]	Class$_{sr}$	d_s	Class$_{d_s}$	$d_{\rm rms}$	Class$_{d_{\rm rms}}$	$\chi^2_{\rm s}$	$\chi^2_{\rm i}$	Class$_{\chi^2}$	
CS 22891−171	0.55	0.37	s/rs	0.48	rs	0.73	s/rs	3.81	1.66	rs	rs
CS 22947−187	0.33	0.46	rs	0.43	rs	0.64	rs	5.78	0.86	rs	rs
HD 145777	0.10	0.02	rs	0.47	rs	0.57	rs	2.01	2.58	s/rs	rs
HD 187861	−0.05	−0.16	r/rs	0.04	r	0.48	rs	6.54	1.78	rs	rs
HD 196944	−0.01	0.24	rs	0.39	rs	0.52	rs	5.04	1.60	rs	rs
HD 224959	0.17	0.19	rs	0.35	rs	0.56	rs	3.29	1.61	rs	rs
SDSS J0912−0216	0.24	−0.27	rs	0.52	rs	0.68	s/rs	19.87	8.29	rs?	rs
SDSS J1349−0229	0.01	−0.29	rs	0.40	rs	0.59	rs	25.81	13.63	rs?	rs
SDSS J1036+1212	0.17	−0.98	rs	0.38	rs	0.72	s/rs	27.79	8.17	rs?	rs
CS 22887−048	0.50	0.42	s	0.63	s/rs	0.75	s	3.69	1.30	rs	s or rs
CS 22942−019	0.51	0.79	s	0.91	s	1.07	s	2.41	1.08	rs	s
CS 29512−073	0.58	0.68	s	0.77	s	0.90	s	3.38	0.88	rs	s
CS 30322−023	0.82	0.64	s	0.83	s	0.97	s	2.60	1.87	rs	s
HD 26	0.92	0.94	s	1.18	s	1.28	s	2.09	1.88	s/rs	s
HD 55496	...	...	...	1.00	s	1.22	s	3.87	6.32	s	s
HD 198269	0.55	0.55	s	0.83	s	0.95	s	1.10	1.17	s/rs	s
HD 206983	0.30	0.27	rs	0.60	s/rs	0.70	s/rs	1.24	0.87	s/rs	s or rs

Note. The three [s/r] columns use both [La/Eu] and [Ba/Eu] to classify the star as s or rs. The four distance columns refer to the distance to the *r*-process, as defined in the text. The star is classified as rs if $d_s \leqslant 0.6$ (respectively, $d_{\rm rms} \leqslant 0.7$). The $\chi^2_{\rm s}$ and $\chi^2_{\rm i}$ indicators evaluate how closely the measured abundances of elements ($Z > 30$) align with the best-fitting theoretical predictions produced by *s*-process and *i*-process AGB models, respectively. When the $\chi^2_{\rm s}$ and $\chi^2_{\rm i}$ are similar and reasonably low, the star is classified as "s/rs" (i.e., the class cannot be securely determined from comparisons to models). A question mark in the class$_{\chi^2}$ column highlights problematic stars with high $\chi^2_{\rm s}$ or $\chi^2_{\rm i}$ values (see the text for details). The "Final Class" column represents the tentative best classification based on the values of various indicators used in this study (d_s, $d_{\rm rms}$, $\chi^2_{\rm s}$, and $\chi^2_{\rm i}$).

companion that transferred material to the secondary star via stellar winds (e.g., T. Masseron et al. 2010 and references therein). The same scenario has been invoked to explain the heavy element enrichment in CEMP-rs stars (e.g., S. Bisterzo et al. 2012; M. Lugaro et al. 2012; C. Abate et al. 2013, 2015; D. Karinkuzhi et al. 2021, 2023; A. Choplin et al. 2024c). To test this hypothesis, the current observations are compared with AGB nucleosynthesis predictions computed using the STAREVOL code (L. Siess et al. 2000; L. Siess & M. Arnould 2008).

In our AGB models, the *s*-process (*i*-process) is followed by a network comprising 414 (1160) nuclei and linked by 639 (2123) reactions. During PIE, the nuclear burning and convective turnover timescales become comparable, so that the nucleosynthesis and transport equations are coupled. We considered AGB models with $M_{\rm ini} = 1$ and $2\,M_\odot$ and $-3 \leqslant$ [Fe/H] $\leqslant -1$. Among these are (1) *s*-process models, representing AGB stars that undergo only *s*-process nucleosynthesis ($2\,M_\odot$ at [Fe/H] $= -1$, -2, -2.5 and -3), and (2) *i*-process models, representing AGB stars that experience *i*-process nucleosynthesis (1 and $2\,M_\odot$ at $-3 \leqslant$ [Fe/H] $\leqslant -1$). While the *i*-process is thought to occur preferentially in low-mass, low-metallicity stars (e.g., Figure 3 in A. Choplin et al. 2022a), it remains unclear which AGB stars undergo *s*-process, *i*-process, or both types of nucleosynthesis. In some cases, varying the mixing parameters within the same stellar model can lead to either *s*- or *i*-process nucleosynthesis. Therefore, both *s*- and *i*-process models were sometimes considered at a given mass and metallicity. Different overshooting strengths $f_{\rm top}$ above the convective thermal pulse were explored in *i*-process models. As discussed in Section 3.2 of A. Choplin et al. (2024c) for a $1\,M_\odot$ AGB model at [Fe/H] $= -2.5$, increasing the value of $f_{\rm top}$ enhances the abundances of elements with $36 \leqslant Z \leqslant 56$ by up to $\sim$1 dex, while simultaneously reducing the abundances of heavier elements with $Z \geqslant 82$ by a similar amount (see also Figure 4(a) in A. Choplin et al. 2024c). Further details about the AGB models are provided in S. Goriely & L. Siess (2018), A. Choplin et al. (2021), D. Karinkuzhi et al. (2021), and A. Choplin et al. (2022a, 2024c).

To fit the chemical abundances of our sample stars with our AGB models, we follow the procedure outlined in Section 6.2 of A. Choplin et al. (2021). For each sample star, the best-fitting AGB nucleosynthesis prediction is identified by minimizing the χ^2 value, representing the quality of the fit (see Equation (7) in A. Choplin et al. 2021). The minimal χ^2 value (representing the difference between the measured and theoretical chemical abundances) is searched by mixing some of the material ejected by our AGB models in the envelope of the companion. During the fitting procedure, the [X/Fe] ratios in our models are obtained by summing the isotopic abundances. The abundance X_i of each isotope i is computed according to the relation

$$X_i = (1 - f)\, X_s + f\, X_{\rm ini}, \tag{4}$$

where X_s and $X_{\rm ini}$ are the surface and initial mass fractions of isotope i, respectively (available since individual isotope abundances are followed in our AGB models). The dilution factor f is a free parameter, varied between 0 and 1 so as to minimize the χ^2 value. It controls the amount of AGB ejecta mixed into the companion envelope.

Only elements heavier than Zn ($Z = 30$) are considered in the χ^2 calculation. Elements with uncertain abundance determinations, including upper limits (listed in Tables B1 and B2, and reported in Figure 6 by gray symbols) are excluded from the χ^2 computation. We note that the number of reliably determined chemical abundances varies from star to star, consequently affecting the number of elements included in the

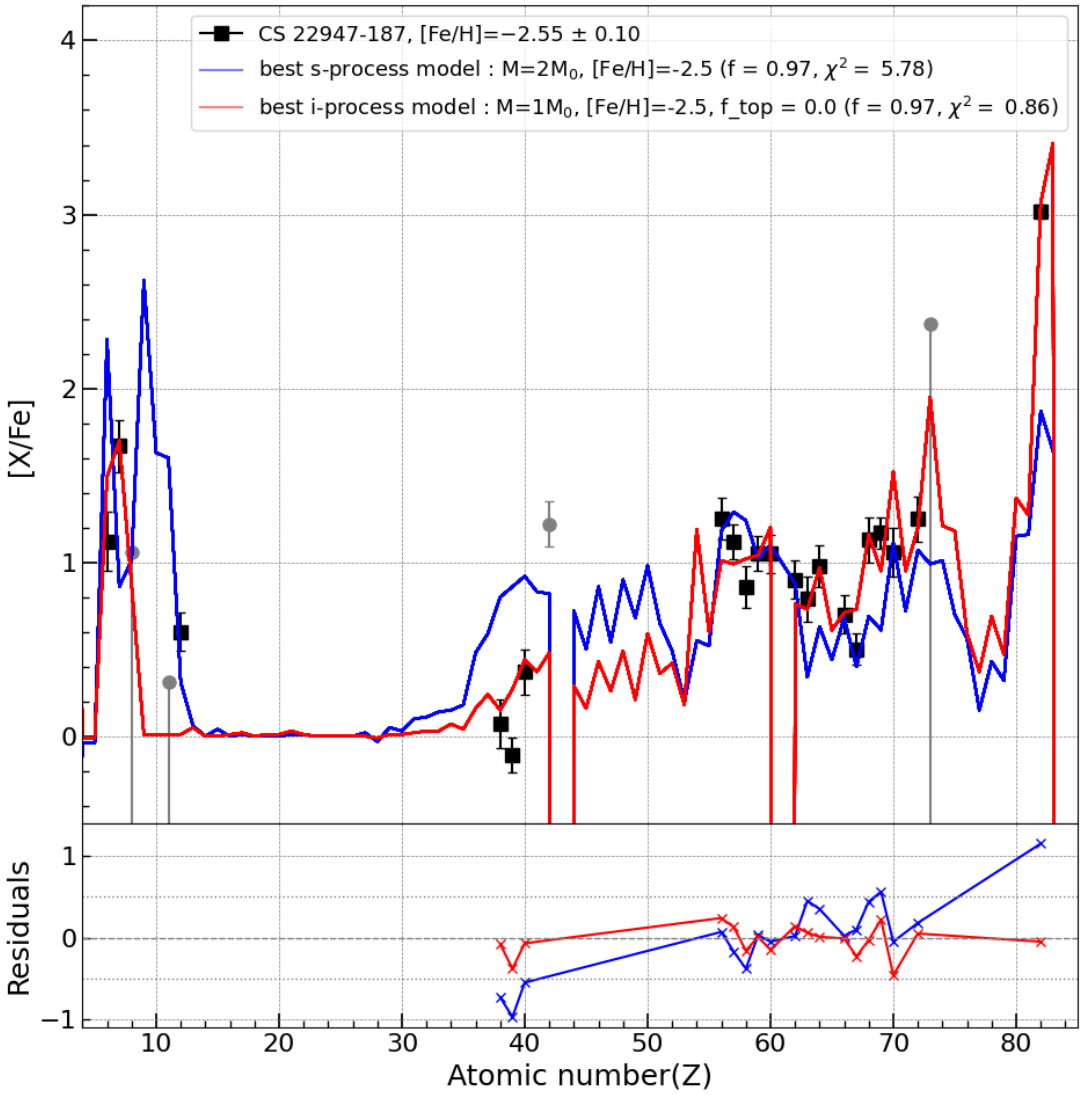

Figure 6. The abundance patterns of the 17 CEMP stars are compared with nucleosynthesis predictions from the STAREVOL code. The measured abundances are indicated by black squares, uncertain abundances by gray circles, and upper limits by gray circles with a downward arrow. In all cases, the best-fitting theoretical predictions for both the *s*-process (blue) and *i*-process (red) are displayed. Only one star is displayed here for reference; the rest are in Appendix C. Models are described in Section 6.

χ^2 calculation. The best-fitting *s*-process (blue pattern) and *i*-process (red pattern) models are illustrated in Figure 6 for one representative star and most extensively in Figure C1 for the full sample.

7. Classification Discussion

We now compare the measured abundance profile with the one predicted from a given nucleosynthesis model (*s*- or *i*-process), for example, with a χ^2 statistic.

First of all, we make the assumption that the secondary star initially has a solar-scaled abundance pattern, i.e., is not enriched in heavy elements, although chemical inhomogeneities are expected in the Galactic halo (e.g., G. Cescutti 2008; B. Wehmeyer et al. 2015). Actually, there is no requirement for the secondary star to follow a solar-scaled abundance pattern at the metallicities of our targets. However, this assumption is legitimate for two reasons. First, we focus on polluted stars that typically exhibit significant heavy element overabundances (+1 to +2 dex). We therefore assume that the pollution dominates any preexisting, possibly nonsolar, abundance patterns. Second, and more importantly, we fit the abundances of the mainly *s*-process elements using either an *s*- or *i*-process model. Since the onset of *s*-process enrichment in the Galaxy occurs relatively late, it is reasonable to assume that the secondary star was not initially enriched in *s*-process elements. We then examine how well this fit reproduces the measured abundances of the mainly *r*-process elements.

χ^2_s (respectively, χ^2_i) values are computed from the best-fitting *s*- or *i*-process models (see Section 6.1), from all available chemical element abundances above Zn after excluding the abundances that are uncertain and have only upper limits, and listed in Table 4. The *s*- or *i*-processes in our AGB models provide a reasonable description of the abundance distributions for most of the program stars (Figures 6 and C1). The resulting classification is listed in the Class$_{\chi^2}$ column in Table 4. Among the 17 CEMP stars analyzed, 6, 12, and 14 stars have χ^2_s or $\chi^2_i \leqslant 1.5$, 2, and 4, respectively (Table 4).

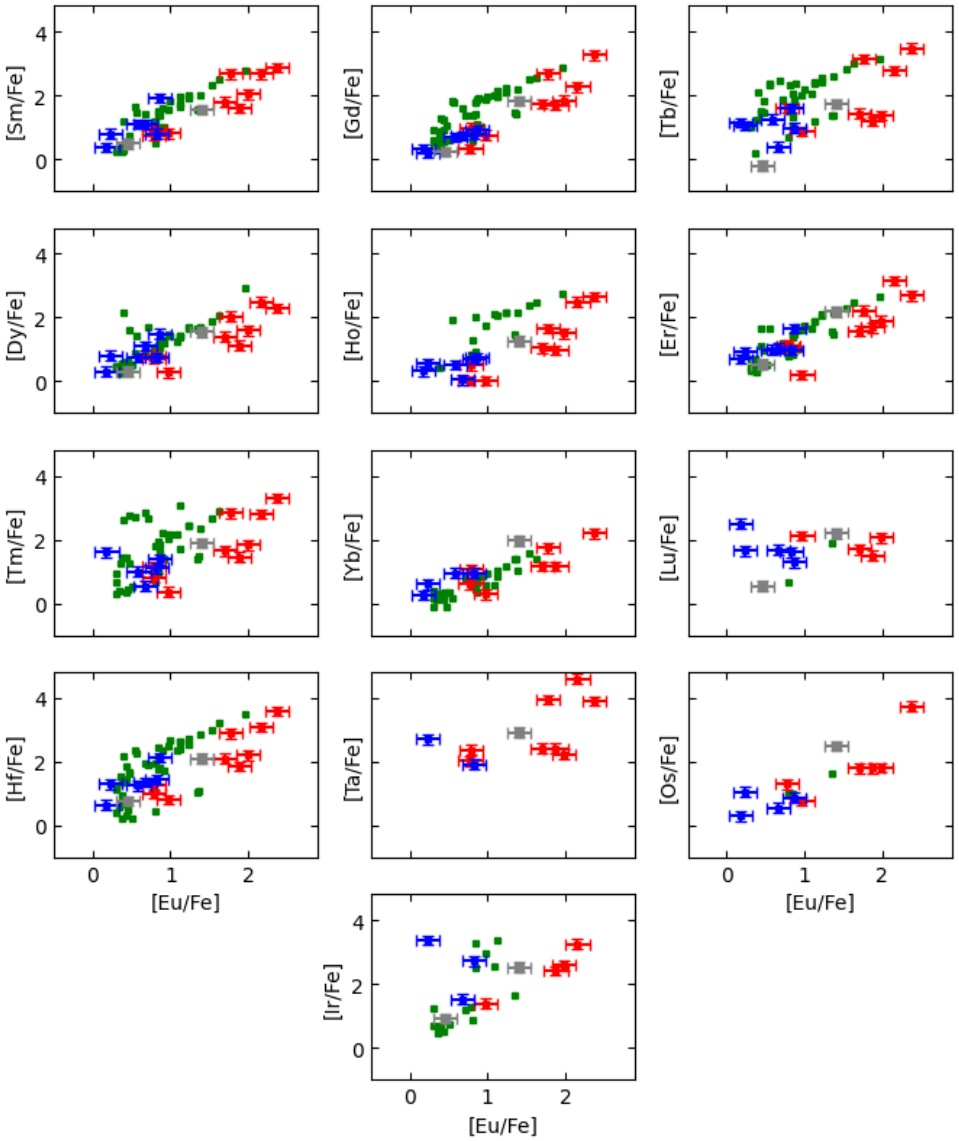

Figure 7. [X/Fe] as a function of [Eu/Fe] for CEMP-rs stars (red squares), CEMP-s stars (blue squares), CEMP stars of uncertain (r or rs) classification (gray squares), and 47 *r*-process enriched stars (some of them are carbon-enriched; green squares) from J. Westin et al. (2000), C. Sneden et al. (2003), I. I. Ivans et al. (2006), and I. U. Roederer et al. (2014). All abundances, including upper limits and uncertain values, were considered.

Except for the two objects CS 22887−048 and HD 206983, all objects in common with K21 remain in the same category. In other words, the newly determined elemental abundances for most stars confirm their K21 CEMP classification. HD 206983 was classified as s in K21; however, its low [La/Eu] and [Ba/Eu] are the main indications of a possible rs assignation. The distance and the χ^2 indicators are rather inconclusive for this star. Similar to the case for CS 22887−048, it was also classified as s in K21 based on the distance measurements. In the present analysis, the d_s and χ^2 measurements put it in the rs class while [La/Eu] and d_{rms} values classify it among the s stars.

One star in particular shows a large dispersion in its light s element abundances: SDSS J1036+1212 has [Sr/Ba] = −1.77 (NLTE) or −1.63 (LTE). Together with [Ba/Fe] = 1.28, this locates it close to the locus of CEMP-rs stars in the diagram [ls/hs] (light s over heavy s) as a function of [hs/Fe]: for example, [Sr/Ba] = f([Ba/Fe]) diagram (C. J. Hansen et al. 2019). Sr is low in SDSS J1036+1212, as well as other light s elements (e.g., [Y/Fe] = 0.87(LTE) to 0.94 (NLTE), though uncertain). However, another ls element shows a much larger abundance: [Zr/Fe] = 1.60, which would place the star among CEMP-s stars and might explain why this star was originally categorized as CEMP-s. However, the other diagnostics, like the [Ba/Eu] or [La/Eu] ratio, and the d_s distance (using eight different heavy element abundances) favor the CEMP-rs classification (the d_{rms} distance is intermediate and inconclusive). Finally, the χ^2 is very large for the *i*-process, but even larger for the *s*-process. Therefore we decided to change this object from the CEMP-s class to the CEMP-rs class.

The 10 stars classified as CEMP-rs with the d_s distance are consistently better fitted (i.e., lower χ^2) by the *i*-process models, except HD 145777, which is nearly equally well fitted by the s- ($\chi^2_s = 2.01$) and *i*-process ($\chi^2_i = 2.58$) models (Table 4). Their residuals (measured-predicted abundances) typically fall within the range of 0.5–1 dex (Figures 6 and C1). This is acceptable

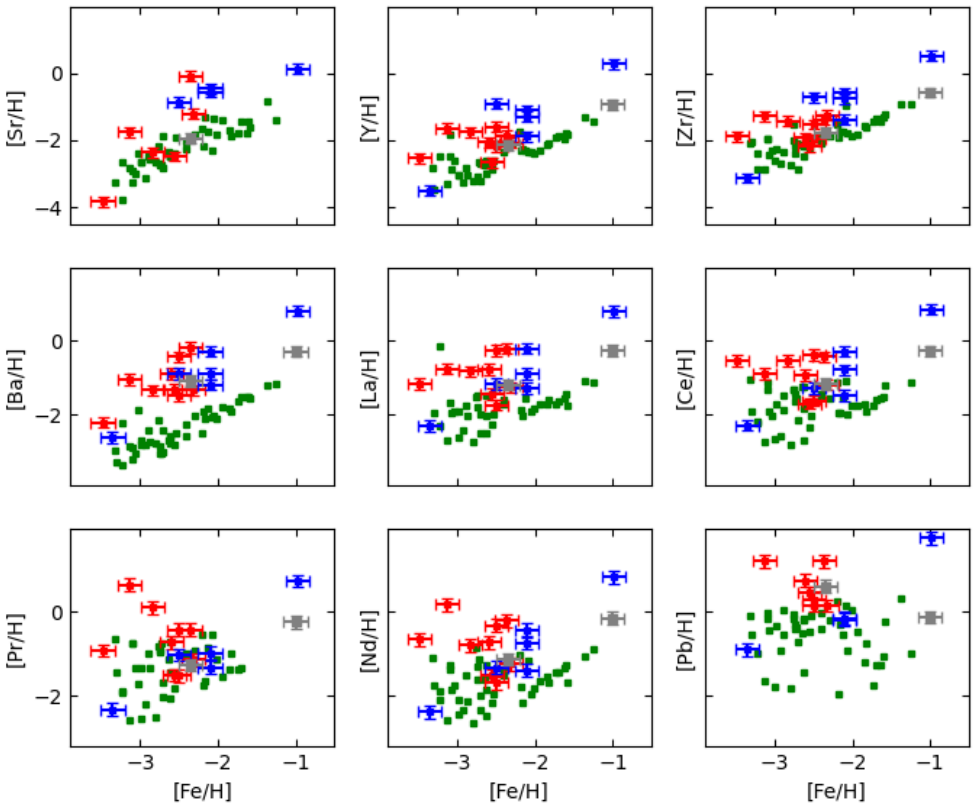

Figure 8. The [s/H] value as a function of [Fe/H] for the mainly-s elements. The red, blue, gray, and green squares have the same meaning as in Figure 7.

given that nuclear uncertainties in *i*-process AGB models are of the same order, i.e., 0.5–1 dex (S. Goriely et al. 2021; S. Martinet et al. 2024). However, the three SDSS stars exhibit a few elements with very high abundances that are challenging to reproduce with our *i*-process models, the most extreme case being Pr ($Z = 59$), which shows an overabundance of 3.8 dex in SDSS J1349−0229. Higher [X/Fe] ratios can be achieved if the PIE occurs when the remaining AGB convective envelope is smaller. As a test, we allowed for dilution in a smaller AGB envelope mass for SDSS J1349−0229 to mimic a late PIE, possibly taking place near the end of the AGB phase or during the post-AGB phase (e.g., F. Herwig et al. 2011; K. De Smedt et al. 2012). In this case, the best-fitting *i*-process model yields $\chi^2_i = 9.2$ (compared to 13.6 when $f = 0$) and successfully reproduces most elemental abundances, with a few notable exceptions such as Ba ($Z = 56$) and Pr ($Z = 59$, Figure C1, red dashed line labeled "late TP"). Notably, the model accounts for the high Ta ($Z = 73$) abundance of approximately 4 dex. Ta is a crucial element for distinguishing between the *s*- and *i*-processes, as its production is significantly higher during *i*-process nucleosynthesis.

In the present study, most of the best-fitting models yield high dilution factors f (see Equation (4)). However, a few stars[6] are better matched by models with low f values. As discussed in A. Choplin et al. (2021) and A. Choplin et al. (2022b), low-dilution factors sometimes imply unrealistically high accreted masses, which may be difficult to reconcile with binary evolution models. These low-dilution cases may therefore raise concerns regarding the required accreted mass. A detailed analysis of this issue is beyond the scope of this paper, but we plan to investigate it in future work.

Surprisingly, three out of the six stars (CS 22942−019, CS 29512−073, and CS 30322−023) classified as s with the d_s distance are better fitted by *i*-process models (we exclude HD 26 because its χ^2_s and χ^2_i are very close, making its χ^2 classification uncertain). These stars have $0.77 \leqslant d_s \leqslant 0.91$, close to the threshold of 0.6 that separates CEMP-rs from CEMP-s stars. For instance, the abundance pattern of two of these stars (CS 29512−073 and CS 22942−019) is better reproduced by our *i*-process models, particularly for elements with $38 \leqslant Z \leqslant 42$ and $Z = 82$ for CS 29512−073. CS 22887−048 is another borderline case, with the d_s and $d_{\rm rms}$ indicators in the borderline region. However, its significant Ta overabundance of ∼3 dex (excluded from the χ^2 calculation due to its uncertainty) is reproduced by the *i*-process model within the error limits but markedly underproduced by the *s*-process model. A more detailed analysis of Ta in this star could provide a clearer classification. We note that considering additional *s*-process AGB models with different initial assumptions (e.g., initial mass) could also potentially reconcile these stars with *s*-process predictions.

8. Comparison of the *R*-process Abundances in Different CEMP Classes

It is important to emphasize that the designation "*r*-process elements" is inherited from their origin in the solar system, where they are predominantly attributed to *r*-process nucleosynthesis. However, in the case of the present paper, as far as CEMP-s and CEMP-rs stars are concerned, these elements are more accurately interpreted as originating from the tail of the *s*- or *i*-process abundance distributions. Indeed, even a

[6] CS 22887-048, HD 26, HD 224959 and the three SDSS stars for *s*-process; SDSS J1036 and SDSS J1349 for *i*-process.

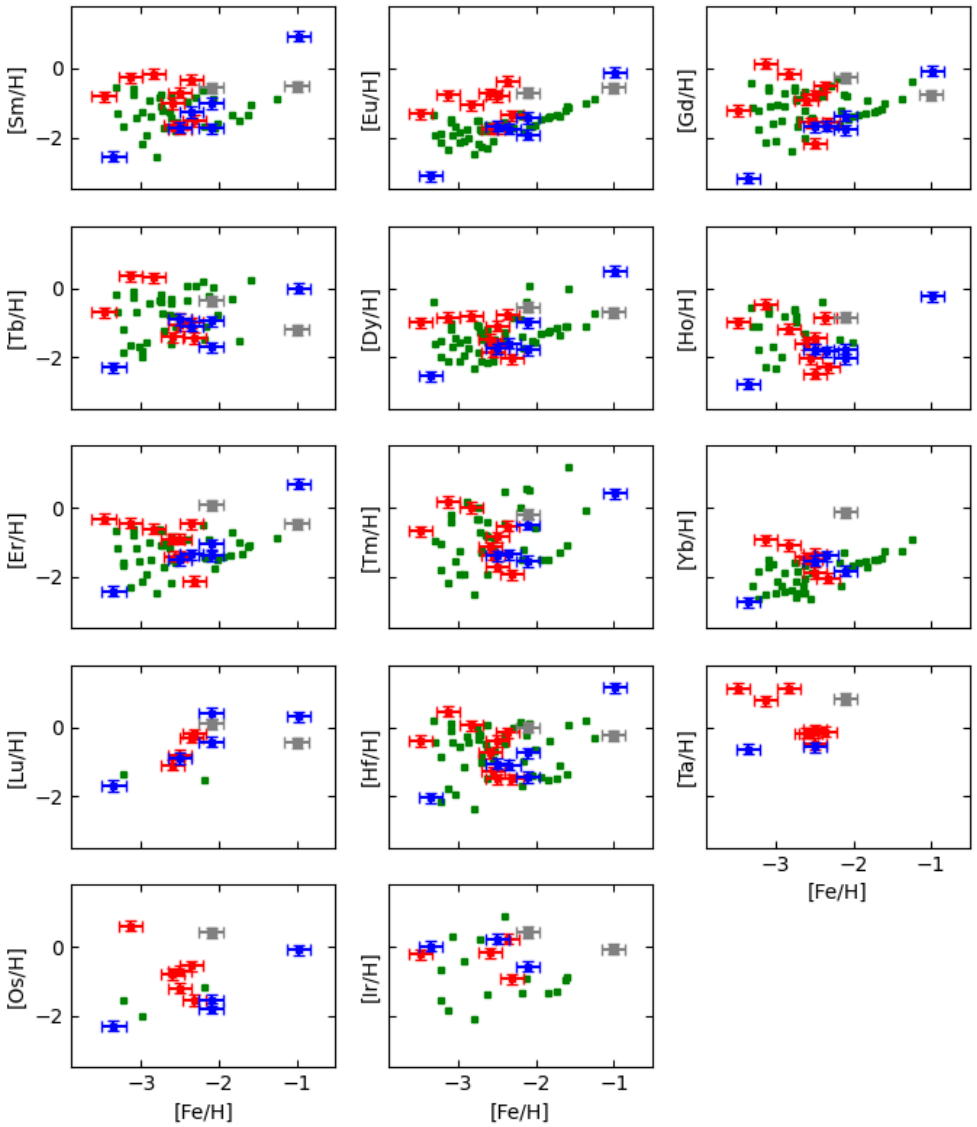

Figure 9. [X/H] as a function of [Fe/H] for mainly-r elements. The red, blue, gray, and green squares have the same meaning as in Figure 7.

standard radiative *s*-process can produce up to 5% of europium, with similarly small yet nonnegligible contributions to other elements typically associated with the *r*-process. In the following, the *r*-process elements produced by the *s* (respectively, *i*) process should be understood as "*s*- (respectively, *i*-) process-made r-elements" (and denoted as r_s or r_i elements for brevity). This nuance is critical when interpreting the measured abundance patterns in these stars.

We now discuss the abundance trends displayed by the different elements.

In Figure 7, we examine the correlations among r-elements (i.e., predominantly attributed to *r*-process nucleosynthesis in the solar system) in CEMP-rs stars, in CEMP-s stars as well as in a sample of *r*-process enriched stars from the literature (J. Westin et al. 2000; C. Sneden et al. 2003; I. I. Ivans et al. 2006; I. U. Roederer et al. 2014). The *r*-process enriched stars considered here are r-I and r-II stars, classified following T. C. Beers & N. Christlieb (2005), with [Eu/Fe] between +0.3 and +1.0 and [Ba/Eu] < 0 for r-I, and [Eu/Fe] $> +1.0$ and [Ba/Eu] < 0 for r-II. Their metallicities ($-4 \leqslant$ [Fe/H] $\leqslant -1$) are similar to those of our CEMP-s and CEMP-rs stars. As expected, most r-elements exhibit a strong correlation with europium, consistent with the hypothesis that they originate from the same astrophysical site. The observed scatter may primarily reflect abundance measurement uncertainties. Notably, the correlation appears weaker for Lu and Ir, which could indicate larger abundance errors for these elements.

We note that in this figure, it is expected to observe an overlap between CEMP-rs and CEMP-s stars. This is because the level of enrichment ([r/Fe]) is independent of the star's classification as CEMP-s or CEMP-rs, which is originally based on abundance ratios such as [La/Eu] or [Ba/Eu] (i.e., [s/r]). For instance, in Figure 7, two CEMP stars are found at very low [r/Fe] enrichment: CS 22942−019 and HD 145777. Nevertheless, CS 22942−019 is classified as a CEMP-s star, as together with its relatively low [Eu/Fe] = 0.83, it exhibits a high [Ba/Fe] = 1.62. In contrast, HD 145777 is categorized as a CEMP-rs star, with [Eu/Fe] = 0.97 and [Ba/Fe] = 0.99.

We now examine the evolution of the mainly s and mainly heavy-r abundances as a function of metallicity (Figures 8 and 9). For mainly s-elements (Figure 8), there is a nice trend of increasing [X/H] with increasing metallicity for CEMP-s and

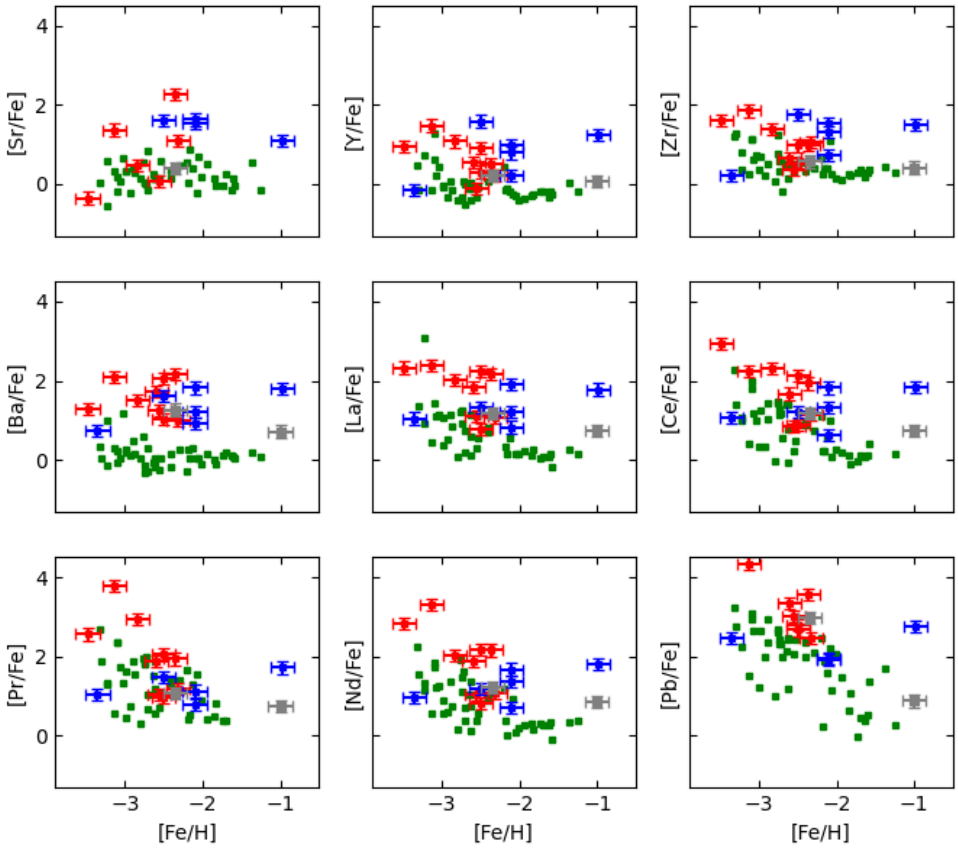

Figure 10. The [s/Fe] as a function of [Fe/H] for the mainly-s elements. The red, blue, gray, and green squares have the same meaning as in Figure 7.

r-process enriched (some of them are carbon-enriched also) stars. For the *r*-process enriched stars, this either reflects the contribution of AGB stars, or the (small) *r*-process contribution to *s*-process elements. Rotating massive stars are also potential contributors to the *s*-process, particularly at low metallicity (e.g., U. Frischknecht et al. 2016). In our sample, however, lead, when measured, is found to be highly overabundant. This is difficult to reconcile with yields from rotating massive stars, which are generally not expected to produce significant amounts of Pb. That said, in stars where lead could not be measured, a contribution from rotating massive stars cannot be ruled out. In CEMP-r stars, the mainly-s elements should therefore reflect the galactic chemical evolution. Indeed, in Figure 10, it can be seen that [X/Fe] (in particular when X = Ce) stays roughly solar from metallicity values between [Fe/H] = −2.0 and −1.0. This is well in line with K. Cunha et al. (2017), who find a constant [Ce/Fe] in field stars from metallicity values between [Fe/H] = −1.0 and 0.0.

CEMP-s stars, obviously, have higher [s/H] abundances than CEMP-r stars. This can be attributed to the nature of the polluting star and to a smaller dilution, since CEMP-s stars have been polluted (after their formation) by a nearby AGB, whereas CEMP-r stars owe their heavy elements to protostellar clouds enriched by one or several events.

However, for CEMP-rs stars, the situation is not as clear. This is further supported by very dispersed Spearman correlation coefficient values between −0.68 (for Pb) and 0.58 (for Sr). The main conclusion is that, based on their dominant *s*-process elements, CEMP-rs stars form a group distinct from both *r*-process enriched and CEMP-s stars. They occupy a region of higher [s/H] than *r*-process enriched stars and lower metallicity than CEMP-s stars. However, the extent to which selection biases (i.e., the identification of a star as CEMP-rs) influence this distinction remains to be assessed.

Similar trends are visible for mainly-r elements (Figure 9), in CEMP-s, -rs, and -r stars. For *r*-process enriched and CEMP-s stars, there is again, for mostly-r elements, a nice trend of increasing [X/H] with increasing [Fe/H]. This reflects the contribution of *r*-process production events (kilonovae, collapsars and MHD SNe) to *r*-process enriched stars. For CEMP-s stars, it might reflect the *r*-process contribution to *r*-process elements, which are present with small abundances in CEMP-s stars.

Again, for CEMP-rs stars, the situation is not that clear: they might show a trend similar to that of *r*-process enriched stars (which would favor an r+s explanation for CEMP-rs stars) or define a different sequence (in which case, their abundance pattern would be due to an event different from the one causing the s- or i-abundance patterns, and also distinct from the one causing the r-pattern). The Spearman correlation coefficient values are similar for CEMP-s and CEMP-r stars, while the negative values in CEMP-rs stars indicate an anticorrelation with metallicity.

In summary, in CEMP-rs stars, the [r/H] ratio appears to increase as metallicity decreases. In contrast, the increase in [r/H] values with metallicity in CEMP-s and *r*-process enriched stars could be due to the galactic chemical evolution.

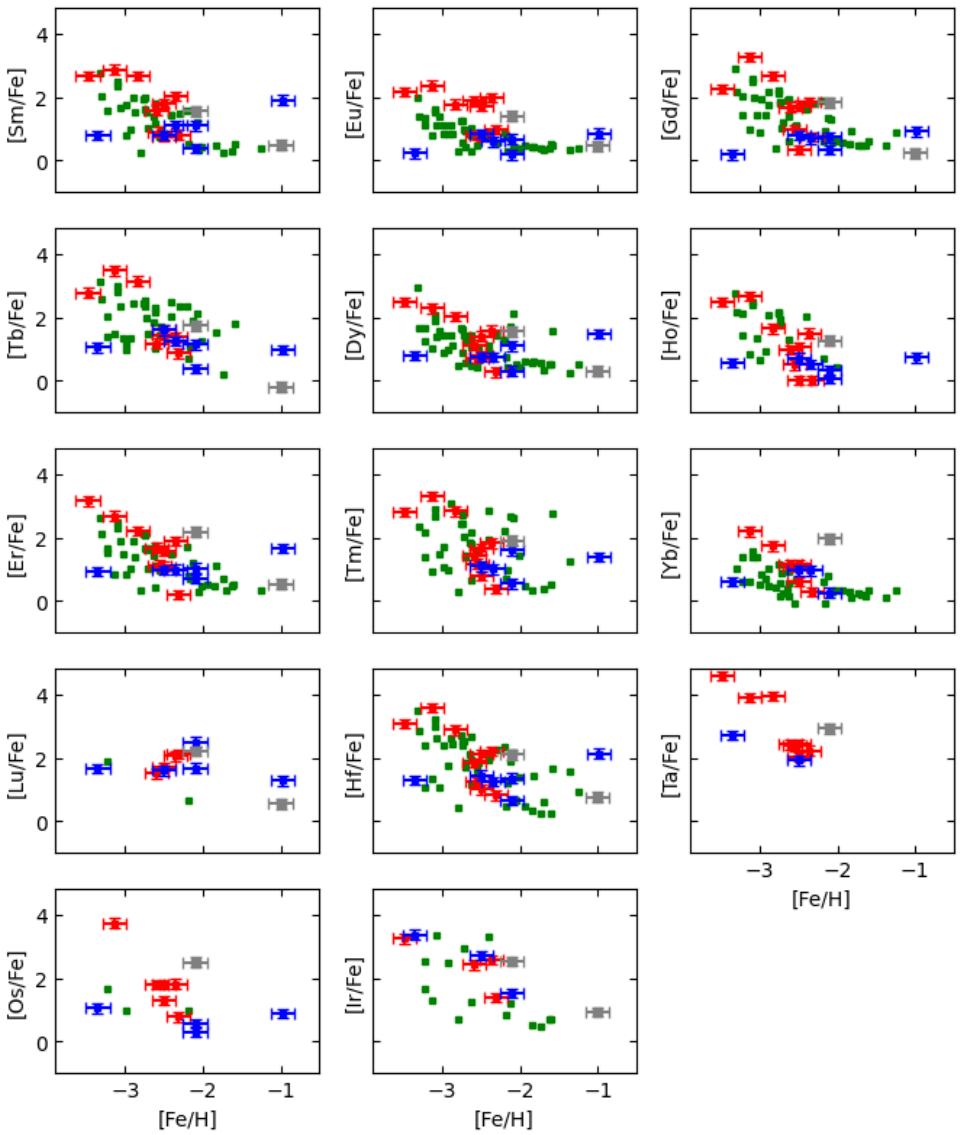

Figure 11. [X/Fe] as a function of [Fe/H] for mainly-r elements. The red, blue, gray, and green squares have the same meaning as in Figure 7.

Figure 11 is well in line with Figure 14 of C. Sneden et al. (2008) and Figure 5 of T. T. Hansen et al. (2018), displaying [Eu/Fe] as a function of [Fe/H]. A large scatter in [Eu/Fe] abundances is observed at low metallicities. C. Sneden et al. (2008, and references therein) suggested it reflects a chemically inhomogeneous early Galaxy. At those early times, enrichment was likely dominated by individual nucleosynthetic events (e.g., supernovae, kilonovae), whose yields were unevenly distributed. As metallicity increases, corresponding to later stages of Galactic evolution, this scatter diminishes, presumably due to the progressive chemical mixing of the interstellar medium. In Figure 12, we present the abundances of elements traditionally classified as *r*-process products as a function of [Mg/H]. The models predict that magnesium is produced in AGB stars with initial masses of 2–3 $M_{\odot}$, but not in stars of 1 $M_{\odot}$, at the metallicities considered. In contrast, the *i*-process is found to operate efficiently in 1 $M_{\odot}$ models, but not in higher-mass stars. Thus, the predictions suggest that low-mass (1 $M_{\odot}$) AGB stars can undergo *i*-process nucleosynthesis without producing significant amounts of Mg, whereas higher-mass stars primarily undergo *s*-process nucleosynthesis, accompanied by Mg production. This trend is consistent with the observational data shown in Figure 12: among CEMP-s stars, a positive correlation is observed between [Mg/H] and the abundances of heavy neutron-capture elements (produced by the *s*-process). In contrast, no such correlation is observed in the presumably lower-mass CEMP-rs stars, which are expected to have experienced the *i*-process but not Mg production. This explanation has to be nuanced by the fact that the stellar evolution and nucleosynthesis models do not take into account any α-enrichment at low metallicity. But at a given metallicity, such an α enrichment should affect CEMP-s and -rs stars in the same way. Since in our sample the metallicity of CEMP-rs stars is, on average, lower than that of CEMP-s stars, this should increase the Mg abundance in CEMP-rs stars, which is not observed. So, neglecting the α enrichment cannot be the cause of the positive correlation (respectively, the absence of correlation) between Mg and heavy neutron-capture elements in CEMP-s stars (respectively, CEMP-rs stars).

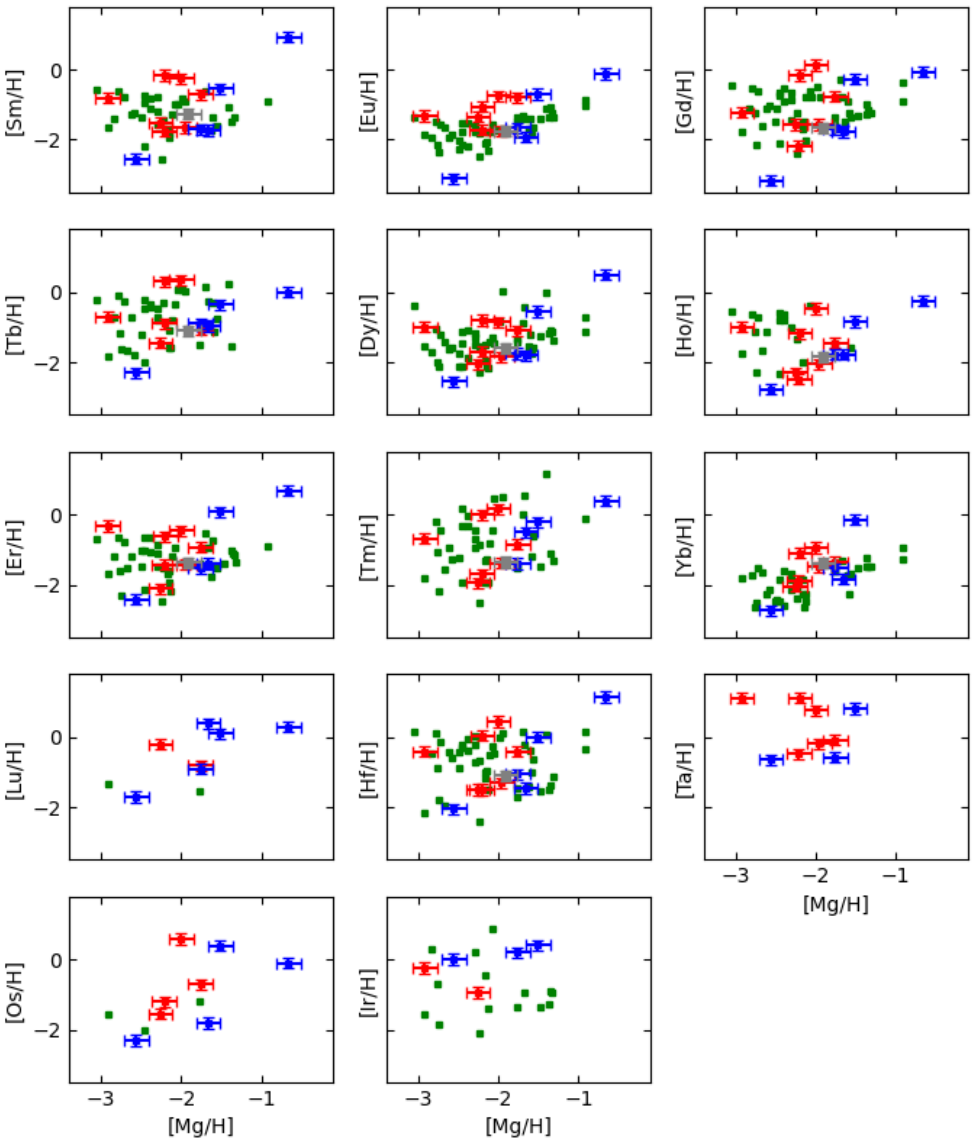

Figure 12. [X/H] as a function of [Mg/H] for *r*-process elements. The red, blue, gray, and green squares have the same meaning as in Figure 7.

9. Conclusions

We used high-resolution UVES spectra for 17 CEMP stars to derive abundances for n-capture elements, focusing on heavy r-elements.

The stars are classified into different CEMP classes with updated abundances, including the NLTE corrections. Several classification indicators were used, in addition to the classical [La/Eu]. In particular, in an attempt to base the classification on a larger number of chemical elements, the model-independent "abundance distances" d_s and $d_{\rm rms}$ suggested by K21 were computed. The agreement with *s*- and *i*-process nucleosynthesis models was also quantified (χ^2_s and χ^2_i).

All of the eight stars initially classified as CEMP-rs stars are confirmed to belong to the CEMP-rs category. Among the nine stars initially classified as CEMP-s stars, six are confirmed and two are classified as "s or rs", essentially because of d_s and $d_{\rm rms}$ distances close to the threshold values 0.6 and 0.7, respectively. In a few stars Tantalum could be tentatively measured, these measurements constitute strong constraints on the operation of the *i*-process. Additionally, the star SDSS J1036+1212, which was initially classified as a CEMP-s star, is now reassigned to the CEMP-rs category, based on its lower [s/r] ratio and d_s value. The systematic comparison of measured abundances with nucleosynthesis model predictions, supported by model-independent abundance-distance diagnostics, provides a more nuanced classification and highlights the need for a multielement approach in disentangling the complex chemical signatures of these stars.

Despite this progress, several open questions remain. What are the precise stellar conditions, such as neutron densities, mixing mechanisms, and progenitor masses, that lead to efficient *i*-process nucleosynthesis in AGB stars? How does the *i*-process vary with metallicity? Furthermore, the detection of elements like Ta, which are rarely measured but sensitive to neutron-capture conditions, raises the question of whether additional, presently unmeasured elements could offer even more definitive diagnostics of the *i*-process.

To address these questions, further high-resolution spectroscopic observations of CEMP stars of various metallicities are crucial. In parallel, advancements in *i*-process modeling, including hydrodynamical simulations, are needed to fully

capture the complexity of the nucleosynthetic environments involved. Expanding the sample of well-characterized CEMP stars with accurate NLTE corrections and full n-capture element coverage will be essential for refining our understanding of the *i*-process and its astrophysical sites.

Acknowledgments

We thank the referee for the insightful remarks that have greatly contributed to the improvement of the paper. M.R. acknowledges the financial support from the UGC, Government of India through the UGC-JRF (NTA Ref. No. 201610156431/CSIR-UGC NET NOVEMBER 2020). D.K. acknowledges the financial support from ANRF through the SURE grant with the file No. (SUR/2022/000748). M.R. and D.K. gratefully acknowledge financial support from Belgium—India project on Precision Astronomical spectroscopy for Stellar and Solar system bodies (BIPASS), approved by the International Division, Department of Science and Technology (DST, Government of India; DST/INT/BELG/P-01/2021 (G)) and the Belgian Federal Science Policy Office (BELSPO, Government of Belgium; BL/33/IN22-BIPASS). A.C. is a Postdoctoral Researcher of the Fonds de la Recherche Scientifique—FNRS. This work is based on observations collected at the European Southern Observatory under ESO program(s) 076.D-0451 and 078.D-0217, obtained from the ESO Science Archive Facility.

Facility: VLT:Kueyen (UVES).

Appendix A
Line List

The atomic lines used for deriving the elemental abundances are presented in Appendix A.

Table A1
Lines Used for Deriving the Elemental Abundances

λ (Å)	χ_{low} (eV)	log *gf*
Na I		
5682.633	2.102	−0.706
5688.205	2.104	−0.450
5889.951	0.000	0.108
5895.924	0.000	−0.144
Mg I		
5528.405	4.346	−0.620
5711.088	4.346	−1.833
Ca I		
5581.965	2.523	−0.555
5588.749	2.526	0.358
5590.114	2.521	−0.571
5594.462	2.523	0.097
5598.480	2.521	−0.087
6102.723	1.879	−0.793
6122.217	1.886	−0.316
6162.173	1.899	−0.090
6169.563	2.526	−0.478
Sc II		
3576.340	0.008	0.007
3613.193	7.877	−2.174
3630.844	7.877	−1.402
4246.822	0.315	0.242
5526.790	1.768	0.024
5641.001	1.500	−1.131
5657.896	1.507	−0.603
Ti I		
5210.385	0.048	−0.884
Ti II		
4411.925	1.224	−2.520
4417.714	1.165	−1.190
4418.330	1.237	−1.970
4441.729	1.180	−2.330
4450.482	1.084	−1.520
4464.449	1.161	−1.810
4468.507	1.131	−0.600
4488.325	3.124	−0.510
4501.270	1.116	−0.770
5211.530	2.590	−1.160
5226.538	1.566	−1.260
5336.771	1.582	−1.590
5381.015	1.566	−1.920
Cr I		
5206.037	0.941	0.020
5208.425	0.941	0.170
5296.691	0.983	−1.360
5298.272	0.983	−1.140
5345.796	1.004	−0.980
5348.315	1.004	−1.290
Cr II		
5237.329	10.760	−0.740
Mn I		
4030.753	0.000	−0.470
4033.062	0.000	−0.618
4034.483	0.000	−0.811
4041.355	2.114	0.285
4783.427	2.298	0.044
4823.524	2.319	0.144
Co I		
4118.767	1.049	−0.490
4121.311	0.923	−0.320
Ni I		
5017.568	3.539	−0.020
5035.357	3.635	0.290
5080.528	3.655	0.330
5081.107	3.847	0.462
5084.089	3.679	0.030
5137.070	1.676	−1.990
5168.656	3.699	−0.430
5476.900	1.826	−0.890
Cu I		
5105.537	1.389	−1.516
5218.197	3.817	0.264
Zn I		
4810.528	4.078	−0.160
Sr II		
3464.453	3.040	0.530
4077.719	0.000	0.170
4215.519	0.000	−0.170
Y II		
4854.863	0.992	−0.111

Table A1
(Continued)

λ (Å)	χ_{low} (eV)	log *gf*
4883.684	1.084	0.265
4900.120	1.033	0.103
5087.416	1.084	−0.170
5200.406	0.992	−0.570
5205.724	1.033	−0.193
Zr II		
3614.765	0.359	−0.252
3751.590	0.972	0.000
3766.795	0.409	−0.830
3836.761	0.559	−0.120
3958.220	0.527	−0.320
3991.127	0.758	−0.310
3998.954	0.559	−0.520
4149.198	0.802	−0.040
4161.200	0.713	−0.590
4208.977	0.713	−0.510
4359.720	1.236	−0.510
5112.270	1.665	−0.850
5350.089	1.827	−1.240
5350.350	1.773	−1.160
Nb II		
3425.425	1.354	−0.140
3426.531	1.315	−0.420
3651.187	0.931	−0.400
Mo I		
3864.103	0.000	−0.010
Ba II		
4130.649	2.722	0.525
4166.000	2.722	−0.433
5853.673	0.604	−0.909
6141.711	0.704	−0.030
6496.895	0.604	−0.406
La II		
4920.965	0.126	−2.261
4920.965	0.126	−2.407
4920.966	0.126	−2.065
4920.966	0.126	−2.078
4920.966	0.126	−2.738
4920.968	0.126	−1.831
4920.968	0.126	−1.956
4920.968	0.126	−2.629
4920.971	0.126	−1.646
4920.971	0.126	−1.895
4920.971	0.126	−2.650
4920.975	0.126	−1.490
4920.975	0.126	−1.891
4920.975	0.126	−2.760
4920.979	0.126	−1.354
4920.979	0.126	−1.957
4920.979	0.126	−2.972
4920.985	0.126	−1.233
4920.985	0.126	−2.162
4920.985	0.126	−3.375
4921.774	0.244	−1.139
4921.774	0.244	−2.220
4921.774	0.244	−3.601
4921.775	0.244	−1.233
4921.775	0.244	−2.005
4921.775	0.244	−3.207
4921.776	0.244	−1.334

Table A1
(Continued)

λ (Å)	χ_{low} (eV)	log *gf*
4921.776	0.244	−1.445
4921.776	0.244	−1.915
4921.776	0.244	−1.927
4921.776	0.244	−2.923
4921.776	0.244	−3.010
4921.777	0.244	−1.566
4921.777	0.244	−1.955
4921.777	0.244	−2.939
4921.778	0.244	−1.700
4921.778	0.244	−1.848
4921.778	0.244	−2.006
4921.778	0.244	−2.053
4921.778	0.244	−2.258
4921.778	0.244	−3.123
4970.386	0.321	−1.160
5290.818	0.000	−1.650
Ce II		
4073.474	0.478	0.230
4081.219	0.478	0.010
4083.222	0.701	0.270
4118.143	0.696	0.190
4127.363	0.684	0.350
4137.645	0.516	0.440
4165.599	0.910	0.530
4222.597	0.122	0.020
4943.840	0.956	−1.000
5274.229	1.044	0.130
5330.556	0.869	−0.400
5353.524	0.879	0.110
6043.373	1.206	−0.480
Pr II		
4000.173	0.204	−0.401
4004.702	0.216	−0.337
4033.830	0.372	−0.128
4044.813	0.000	−0.311
4056.534	0.630	0.353
4062.805	0.422	0.330
4100.717	0.550	0.572
5219.045	0.795	−0.053
5220.108	0.796	0.298
5259.728	0.633	0.114
5322.772	0.483	−0.141
Nd II		
4446.380	0.205	−0.350
4451.560	0.380	0.070
4797.150	0.559	−0.690
4914.380	0.380	−0.700
4959.115	0.064	−0.800
5089.832	0.205	−1.160
5092.788	0.380	−0.610
5123.779	0.380	−0.610
5130.586	1.304	0.450
5132.328	0.559	−0.710
5192.610	1.136	0.270
5249.576	0.976	0.200
5255.502	0.205	−0.670
5273.427	0.680	−0.180
5276.869	0.859	−0.440
5293.160	0.823	0.100
5311.450	0.986	−0.420
5319.810	0.550	−0.140
5361.467	0.680	−0.370

Table A1
(Continued)

λ (Å)	χ_{low} (eV)	log *gf*
Sm II		
3941.876	0.000	−0.860
4064.579	0.248	−0.676
4318.926	0.277	−0.250
4390.854	0.185	−0.450
4420.520	0.333	−0.430
4424.337	0.485	0.140
4433.890	0.434	−0.190
4434.318	0.378	−0.070
4452.720	0.277	−0.410
4467.340	0.659	0.150
4815.800	0.185	−0.820
Eu II		
3819.577	0.000	−0.620
3819.594	0.000	−0.511
3819.596	0.000	−1.289
3819.618	0.000	−0.402
3819.620	0.000	−1.099
3819.622	0.000	−2.507
3819.648	0.000	−0.297
3819.651	0.000	−1.045
3819.654	0.000	−2.361
3819.684	0.000	−0.198
3819.689	0.000	−1.087
3819.693	0.000	−2.448
3819.727	0.000	−0.105
3819.733	0.000	−1.277
3819.738	0.000	−2.776
3907.046	0.207	−0.374
3907.080	0.207	−0.542
3907.093	0.207	−1.186
3907.108	0.207	−0.742
3907.119	0.207	−1.020
3907.131	0.207	−0.994
3907.132	0.207	−2.283
3907.138	0.207	−1.010
3907.147	0.207	−1.358
3907.149	0.207	−1.918
3907.152	0.207	−1.096
3907.159	0.207	−1.772
3907.160	0.207	−1.261
3907.165	0.207	−1.805
3930.424	0.207	−1.219
3930.429	0.207	−0.326
3930.469	0.207	−1.044
3930.472	0.207	−0.534
3930.477	0.207	−1.219
3930.506	0.207	−1.022
3930.507	0.207	−0.771
3930.510	0.207	−1.044
3930.535	0.207	−1.098
3930.536	0.207	−1.040
3930.538	0.207	−1.022
3930.556	0.207	−1.307
3930.557	0.207	−1.316
3930.558	0.207	−1.098
3930.569	0.207	−1.404
3930.570	0.207	−1.307
3971.892	0.207	−0.316
3971.894	0.207	−1.328
3971.896	0.207	−2.650
3971.942	0.207	−0.436
3971.944	0.207	−1.145

Table A1
(Continued)

λ (Å)	χ_{low} (eV)	log *gf*
3971.945	0.207	−2.307
3971.984	0.207	−0.567
3971.985	0.207	−1.111
3971.986	0.207	−2.198
3972.016	0.207	−0.713
3972.017	0.207	−1.170
3972.017	0.207	−2.307
3972.039	0.207	−0.876
3972.039	0.207	−1.353
3972.052	0.207	−1.052
4129.600	0.000	−1.512
4129.604	0.000	−1.035
4129.617	0.000	−1.316
4129.622	0.000	−0.977
4129.626	0.000	−1.512
4129.642	0.000	−1.257
4129.648	0.000	−0.847
4129.653	0.000	−1.316
4129.675	0.000	−1.294
4129.682	0.000	−0.696
4129.688	0.000	−1.257
4129.717	0.000	−1.480
4129.724	0.000	−0.545
4129.730	0.000	−1.294
4129.774	0.000	−0.401
4129.781	0.000	−1.480
4204.896	0.000	−1.112
4204.899	0.000	−1.413
4204.904	0.000	−2.367
4204.921	0.000	−0.936
4204.927	0.000	−1.230
4204.934	0.000	−2.258
4204.958	0.000	−0.773
4204.965	0.000	−1.171
4204.974	0.000	−2.367
4205.006	0.000	−0.627
4205.015	0.000	−1.205
4205.026	0.000	−2.710
4205.065	0.000	−0.496
4205.076	0.000	−1.388
4205.135	0.000	−0.376
Gd II		
3362.239	0.079	0.430
3545.790	0.144	0.190
3549.359	0.240	0.290
3646.195	0.240	0.320
3671.205	0.079	−0.220
3719.452	1.233	0.460
3768.396	0.079	0.360
3844.578	0.144	−0.400
4077.966	0.103	−0.040
4215.022	0.427	−0.440
4251.731	0.382	−0.220
4342.181	0.600	−0.270
3845.633	0.790	0.252
3899.188	0.373	0.330
3939.539	0.000	−0.270
4002.566	0.641	0.100
4005.467	0.126	−0.020
Tb II		
3625.510	0.401	−0.060
3658.888	0.126	−4.083

Table A1
(Continued)

λ (Å)	χ_{low} (eV)	log *gf*
3702.869	0.126	−1.671
3775.268	0.790	−0.570
Dy II		
3407.796	0.000	0.180
3445.570	0.000	−0.150
3538.519	0.000	−0.020
3645.398	0.103	0.340
3944.680	0.000	0.110
4000.450	0.103	0.040
4073.120	0.538	−0.320
4077.966	0.103	−0.040
4103.306	0.103	−0.380
Ho II		
3453.123	0.079	−0.930
3456.020	0.000	−2.828
3484.816	0.079	−0.636
3676.358	0.126	0.480
3747.380	0.401	0.130
3796.754	0.000	−1.722
3810.738	0.000	0.142
4045.470	0.000	−0.918
4152.586	0.079	−2.733
Er II		
3524.913	0.000	−0.887
3692.649	0.055	0.138
3729.524	0.000	−0.488
3830.481	0.000	−0.365
3896.233	0.055	−0.241
3906.311	0.000	−0.052
Tm II		
3700.255	0.029	−0.380
3701.362	0.000	−0.540
3734.123	0.029	−0.710
3761.958	3.328	−2.850
3795.759	0.029	−0.230
3848.019	0.000	−0.140
3958.097	0.000	−1.120

Table A1
(Continued)

λ (Å)	χ_{low} (eV)	log *gf*
Yb II		
3694.192	0.000	−0.300
Lu II		
3507.395	0.000	−1.637
5983.701	1.462	−1.952
6221.592	1.541	−2.471
Hf II		
3399.790	0.000	−0.570
3505.219	1.037	−0.140
3719.276	0.608	−0.810
3793.379	0.378	−1.110
3918.090	0.452	−1.140
4093.150	0.452	−1.150
Ta II		
3379.507	0.511	−0.520
3406.666	0.847	−0.110
3414.128	0.847	−0.210
3440.312	1.797	0.540
3446.851	1.575	0.240
3541.882	0.128	−1.140
3573.407	1.459	0.340
3694.501	1.797	0.150
Os I		
4260.849	0.000	−1.434
4420.477	0.000	−1.590
Ir I		
3725.392	2.363	−0.430
3738.530	0.784	−2.070
3747.205	0.717	−1.480
3768.673	1.467	−1.600
3800.120	0.000	−1.450
3951.948	1.515	−1.570
3992.121	1.225	−1.220
Pb I		
4057.832	1.320	−0.220

Appendix B
Elemental Abundances for the Program Stars

Elemental abundances for the program stars analysed in this work are presented in Table B1.

Table B1
Elemental Abundances

			CS 22947−187				CS 29512−073			
	Z	$\log_{\odot}\epsilon$[a]	log ϵ	σ_l (N)	[X/Fe] $\pm$ σ_t	[X/Fe][b]	log ϵ	σ_l(N)	[X/Fe] $\pm$ σ_t	[X/Fe][b]
C	6	8.43	7.00	0.10(1)	1.12 ± 0.17	1.26	7.45	0.10(1)	1.37 ± 0.17	1.05
$^{12}C/^{13}C$[f]					1.5 ± 0.3				19 ± 8.8	
$^{12}C/^{13}C$[g]					2.3 ± 0.7				11.5 ± 1.9	
N	7	7.83	6.95	0.10(1)	1.67 ± 0.15	1.71	6.10	0.10(1)	0.62 ± 0.15	0.40
O	8	8.69	7.20[e]	0.10(1)	1.06[e] ± 0.16	0.62	8.60[c]	0.10(1)	2.26[c] ± 0.16	0.42
Na	11	6.24	4.00[e]	0.10(1)	0.31[e] ± 0.13	0.16	4.05[d]	0.05(2)	0.16[d] ± 0.09	
Mg	12	7.66	5.70	0.10(2)	0.59 ± 0.11	0.56	5.75	0.10(2)	0.44 ± 0.11	0.01
Ca	20	6.34	4.25	0.03(9)	0.46 ± 0.08	0.51	4.33	0.05(6)	0.34 ± 0.08	0.25
Sc	21	3.15	0.75	0.05(2)	0.15 ± 0.11	0.11	0.71	0.10(2)	−0.09 ± 0.13	−0.21
Ti	22	4.95	2.74	0.09(13)	0.34 ± 0.10	0.32	2.83	0.04(6)	0.23 ± 0.10	0.06
Cr	24	5.64	3.06	0.07(7)	−0.03 ± 0.09	−0.06	3.15	0.05(4)	−0.14 ± 0.09	−0.14
Mn	25	5.43	2.60	0.10(1)	−0.28 ± 0.13	−0.21	2.74	0.10(5)	−0.34 ± 0.10	−0.44
Fe	26	7.50	4.95	0.07(81)			5.15	0.07(91)		
Co	27	4.99	2.60	0.10(2)	0.16 ± 0.12	−0.05	2.60	0.10(2)	−0.04 ± 0.12	−0.24
Ni	28	6.22	3.80	0.06(6)	0.13 ± 0.09	0.17	3.88	0.07(7)	0.01 ± 0.09	0.06
Zn	30	4.56	2.30	0.10(1)	0.29 ± 0.13	0.27	2.50	0.10(1)	0.29 ± 0.13	0.11
Sr_{LTE}	38	2.87	0.40	0.10(1)	0.08 ± 0.14	0.29	0.95	0.10(1)	0.43 ± 0.15	0.31
Sr_{NLTE}	38	2.87	0.39	0.10(1)	0.07 ± 0.14		0.92	0.10(1)	0.40 ± 0.15	
Y_{LTE}	39	2.21	−0.57	0.05(6)	−0.23 ± 0.10	−0.14	−0.05	0.06(5)	0.09 ± 0.11	0.21
Y_{NLTE}	39	2.21	−0.45	0.05(6)	−0.11 ± 0.10		0.07	0.06(5)	0.21 ± 0.11	
Zr	40	2.58	0.40	0.10(7)	0.37 ± 0.13	0.34	0.80	0.10(2)	0.57 ± 0.11	0.50
Nb	41	1.46	...	...	...		0.70[c]	0.10(1)	1.59[c] ± 0.12	
Mo	42	1.88	0.55[c]	0.10(1)	1.22[c] ± 0.13	1.45	0.40	0.10(1)	0.87 ± 0.13	1.18
Ba	56	2.18	0.88	0.08(3)	1.25 ± 0.12	1.53	1.10	0.13(3)	1.27 ± 0.13	1.44
La	57	1.10	−0.33	0.04(4)	1.12 ± 0.10	0.96	−0.08	0.03(2)	1.17± 0.11	1.04
Ce	58	1.58	−0.11	0.07(11)	0.86 ± 0.12	0.89	0.42	0.03(9)	1.19 ± 0.10	1.26
Pr	59	0.72	−0.78	0.08(5)	1.05 ± 0.10	0.95	−0.54	0.05(7)	1.09 ± 0.09	1.09
Nd	60	1.42	−0.08	0.05(6)	1.05 ± 0.11	1.04	0.30	0.05(9)	1.23 ± 0.10	1.21
Sm	62	0.96	−0.69	0.08(4)	0.90 ± 0.11	0.73	−0.30	0.06(5)	1.09 ± 0.10	0.86
Eu_{LTE}	63	0.52	−1.36	0.15(4)	0.67 ± 0.12	0.56	−1.32	0.14(5)	0.51 ± 0.11	0.36
Eu_{NLTE}	63	0.52	−1.24	0.10(1)	0.79 ± 0.13		−1.24	0.14(1)	0.59 ± 0.11	
Gd	64	1.07	−0.50	0.10(2)	0.98 ± 0.12	0.91	−0.59	0.12(5)	0.69 ± 0.15	
Tb	65	0.30	...	...	...		−0.80[d]	0.10(1)	1.25[d] ± 0.11	1.83
Dy	66	1.10	−0.75	0.10(2)	0.70 ± 0.11	0.61	−0.50	0.10(4)	0.75 ± 0.15	0.88
Ho	67	0.48	−1.57	0.03(2)	0.50 ± 0.09	0.79	−1.36[c]	0.05(3)	0.51[c] ± 0.09	
Er	68	0.92	−0.50	0.09(3)	1.13 ± 0.13	1.00	−0.44	0.09(4)	0.99 ± 0.13	0.89
Tm	69	0.10	−1.28	0.04(3)	1.17 ± 0.09		−1.25[d]	0.05(2)	1.00[d] ± 0.10	1.98
Yb	70	0.84	−0.65	0.10(1)	1.06 ± 0.14	1.38	−0.55[c]	0.10(1)	0.96[c] ± 0.14	1.05
Hf	72	0.85	−0.45	0.05(2)	1.25 ± 0.13	1.28	−0.25[e]	0.05(2)	1.25[e] ± 0.13	1.56
Ta	73	−0.12	−0.30[e]	0.10(3)	2.37[e] ± 0.11		...	...	...	
Pb_{LTE}	82	1.75	1.85	0.10(1)	2.65 ± 0.04	2.33	1.85	0.10(1)	2.45 ± 0.04	2.07
Pb_{NLTE}	82	1.75	2.22	0.10(1)	3.02 ± 0.04		2.37	0.10(1)	2.97 ± 0.04	

Table B1
(Continued)

			SDSSJ 0912+0216				SDSSJ 1036+1212				SDSS J1349−0229			
	Z	$\log_{\odot}\epsilon$[a]	$\log\epsilon$	σ_l (N)	[X/Fe] $\pm\ \sigma_t$	[X/Fe][b]	$\log\epsilon$	σ_l(N)	[X/Fe] $\pm\ \sigma_t$	[X/Fe][b]	$\log\epsilon$	σ_l(N)	[X/Fe] $\pm\ \sigma_t$	[X/Fe][b]
C	6	8.43	7.70	0.10(1)	2.10 ± 0.17	2.17	6.30	0.10(1)	1.35 ± 0.17	1.47	8.20	0.10(1)	2.90 ± 0.17	2.82
$^{12}C/^{13}C$[f]					11.5 ± 1.9				4 ± 1.5				5.6 ± 1.4	
$^{12}C/^{13}C$[g]					9 ± 3.1				5.6 ± 1.4				5.6 ± 1.4	
N	7	7.83	6.85	0.10(1)	1.85 ± 0.15	1.75	6.40[c]	0.10(1)	2.05[c] ± 0.15	1.29	6.80	0.10(1)	2.10 ± 0.15	1.60
Na	11	6.24	4.40[e]	0.10(2)	0.99[e] ± 0.13	0.38	3.40	0.10(2)	0.64 ± 0.19	0.43				
Mg	12	7.60	5.40	0.10(1)	0.63 ± 0.13	0.21	4.70[c]	0.10(1)	0.56[c] ± 0.13	0.00	5.60	0.10(1)	1.13 ± 0.13	0.57
Ca	20	6.34	4.00	0.10(3)	0.49 ± 0.11	0.42	3.33	0.05(3)	0.47 ± 0.09	0.38	3.80[c]	0.10(2)	0.59[c] ± 0.11	0.40
Sc	21	3.15	0.78	0.13(3)	0.46 ± 0.13	0.28	−0.30	0.11(3)	0.03 ± 0.13	0.11	0.59	0.12(4)	0.57 ± 0.13	
Ti	22	4.95	2.70	0.04(3)	0.58 ± 0.10	0.51	2.10	0.05(2)	0.63 ± 0.11	0.75	2.50	0.04(3)	0.68 ± 0.10	0.55
Cr	24	5.64	2.70	0.08(3)	−0.11 ± 0.09	−0.16	2.10	0.10(2)	−0.06 ± 0.11	−0.12	2.80	0.08(3)	0.29 ± 0.09	−0.02
Mn	25	5.43	2.10	0.10(2)	−0.50 ± 0.12	−0.55	1.27	0.05(3)	−0.68 ± 0.09		2.20	0.10(2)	−0.10 ± 0.13	−0.68
Fe	26	7.50	4.67	0.07(67)			4.02	0.07(52)			4.37	0.07(52)		
Co	27	4.99	2.65	0.10(2)	0.49 ± 0.12	0.31	1.90	0.10(1)	0.39 ± 0.14	0.57	...	...	...	
Ni	28	6.22	4.20[e]	0.18(4)	0.81[e] ± 0.12	0.07	3.60	0.05(2)	0.86 ± 0.09	0.28	...	...	...	
Cu	29	4.19	...	...	...		1.60	0.10(1)	0.89 ± 0.14		3.00[c]	0.10(1)	1.94[c] ± 0.14	
Zn	30	4.56	2.30[e]	0.10(1)	0.57[e] ± 0.13		1.70[e]	0.10(1)	0.62 ± 0.13		2.70[c]	0.10(1)	1.27[c] ± 0.13	
Sr_{LTE}	38	2.87	0.50	0.10(2)	0.46 ± 0.14	0.57	−1.10	0.10(1)	−0.49 ± 0.14	−0.56	1.10	0.10(2)	1.36 ± 0.15	1.30
Sr_{NLTE}	38	2.87	0.51	0.10(2)	0.47 ± 0.14		−0.96	0.10(1)	−0.35 ± 0.14		1.11	0.10(2)	1.37 ± 0.15	
Y_{LTE}	39	2.21	0.35	0.05(2)	0.97 ± 0.14	0.61	−0.40[e]	0.10(2)	0.87[e] ± 0.12	0.24	0.50	0.17(4)	1.42 ± 0.13	1.29
Y_{NLTE}	39	2.21	0.46	0.05(2)	1.08 ± 0.14		−0.33[e]	0.10(2)	0.94[e] ± 0.12		0.56	0.17(4)	1.48 ± 0.13	
Zr	40	2.58	1.15[e]	0.08(4)	1.40[e] ± 0.13	1.08	0.70	0.10(3)	1.60 ± 0.13	1.02	1.30[c]	0.10(4)	1.850[c] ± 0.13	1.56
Nb	41	1.46	...	...	...		0.70[c]	0.10(1)	2.72[c] ± 0.12		2.05[c]	0.05(2)	3.72[c] ± 0.12	
Mo	42	1.88	1.40[c]	0.10(1)	2.35[c] ± 0.13		0.30	0.10(1)	1.90 ± 0.13		1.58[d]	0.10(1)	2.83[d] ± 0.13	
Ba	56	2.18	0.85	0.05(3)	1.50 ± 0.11	1.49	−0.02	0.12(2)	1.28 ± 0.15	1.17	1.13	0.08(3)	2.08 ± 0.15	2.17
La	57	1.10	0.28[c]	0.03(2)	2.01[c] ± 0.11	1.35	−0.05	0.10(2)	2.33 ± 0.13	2.39	0.35[c]	0.05(2)	2.38[c] ± 0.15	1.74
Ce	58	1.58	1.05	0.05(2)	2.30 ± 0.12	2.17	1.04[c]	0.28(3)	2.94[c] ± 0.19	2.32	0.70	0.10(1)	2.25 ± 0.14	2.63
Pr	59	0.72	0.83	0.07(3)	2.94 ± 0.17	2.25	−0.20[e]	0.10(2)	2.56[e] ± 0.13	2.45	1.37	0.13(4)	3.78 ± 0.13	2.87
Nd	60	1.42	0.63	0.12(3)	2.04 ± 0.12	1.12	0.77	0.18(3)	2.83 ± 0.14	2.08	1.60[c]	0.11(5)	3.31[c] ± 0.11	1.91
Sm	62	0.96	0.80[e]	0.10(1)	2.67[c] ± 0.12	2.60	0.15	0.12(2)	2.67 ± 0.14	2.92	0.70	0.10(3)	2.87 ± 0.14	2.35
Eu_{LTE}	63	0.52	−0.67	0.14(3)	1.64 ± 0.12	1.20	−0.85	0.10(2)	2.11 ± 0.11	1.26	−0.14	0.15(2)	2.47 ± 0.13	1.62
Eu_{NLTE}	63	0.52	−0.54	0.14(3)	1.77 ± 0.12		−0.80	0.10(2)	2.16 ± 0.11		−0.24	0.10(1)	2.37 ± 0.13	
Gd	64	1.07	0.91	0.09(2)	2.67 ± 0.15	2.80	−0.15	0.11(2)	2.26 ± 0.15	2.62	1.20	0.12(4)	3.26 ± 0.15	2.50
Tb	65	0.30	0.61	0.05(2)	3.14 ± 0.11	2.64	−0.40[c]	0.10 (2)	2.78[c] ± 0.12	2.90	0.65[c]	0.10(1)	3.48[c] ± 0.15	2.69
Dy	66	1.10	0.30	0.10(2)	2.03 ± 0.15	1.96	0.10	0.10(3)	2.48 ± 0.15	2.46	0.25	0.10(1)	2.28 ± 0.13	2.39
Ho	67	0.48	−0.70	0.10(1)	1.65 ± 0.12		−0.52	0.08(3)	2.48 ± 0.10		0.01[c]	0.14(2)	2.66[c] ± 0.12	
Er	68	0.92	0.30	0.10(1)	2.21 ± 0.16	2.03	0.60[c]	0.10(1)	3.16[c] ± 0.16	2.86	0.47[c]	0.15(2)	2.68[c] ± 0.16	2.73
Tm	69	0.10	0.10	0.10(1)	2.83 ± 0.13		−0.58	0.09(2)	2.80 ± 0.05	2.78	0.27[c]	0.15(2)	3.30[c] ± 0.14	
Yb	70	0.84	−0.25	0.10(1)	1.74 ± 0.14		⋯	⋯	⋯		−0.10[c]	0.10(1)	2.19[c] ± 0.14	
Hf	72	0.85	0.90[e]	0.10(1)	2.88[e] ± 0.15	2.72	0.45[e]	0.10(1)	3.08[e] ± 0.15	2.35	1.30[c]	0.10(2)	3.58[c] ± 0.16	3.14
Ta	73	−0.12	1.00[e]	0.10(1)	3.95[e] ± 0.13		1.00[e]	0.15(2)	4.60[e] ± 0.14		0.65[c]	0.10(1)	3.90[c] ± 0.13	
Os	76	1.40	...	...	...			...	...	...	2.00[c]	0.10(1)	3.73[c] ± 0.15	
Ir	77	1.38	...	...	...		1.50[d]	0.10(1)	3.25[d] ± 0.11		...	...	...	
Pb_{LTE}	82	1.75	...	...	...			...	...	...	2.35[c]	0.10(1)	3.73[c] ± 0.04	3.09
Pb_{NLTE}	82	1.75	...	...	...			...	...	...	2.97[c]	0.10(1)	4.35[c] ± 0.04	

Notes.
[a] M. Asplund et al. (2009).
[b] I. U. Roederer et al. (2014), N. T. Behara et al. (2010) (For the three SDSS stars).
[c] Uncertain abundances due to noisy/blended region.
[d] Very uncertain abundances due to noisy/blended region.
[e] Upper limit and uncertain.
[f] $^{12}C/^{13}C$ ratio from CH *G* band.
[g] $^{12}C/^{13}C$ ratio from CN band.

Table B2
Elemental Abundances of the Objects from D. Karinkuzhi et al. (2021)

			CS 22887−048			CS 22891−171			HD 145777		
	Z	$\log_{\odot}\epsilon$[a]	log ϵ	σ_t(N)	[X/Fe] $\pm$ σ_t	log ϵ	σ_t(N)	[X/Fe] $\pm$ σ_t	log ϵ	σ_t(N)	[X/Fe] $\pm$ σ_t
Gd	64	1.07	0.80[b]	0.10(1)	1.83[c] $\pm$ 0.15	0.30[b]	0.10(1)	1.73 $\pm$ 0.17	−0.50[b]	0.10(1)	0.75 $\pm$ 0.17
Tb	65	0.30	−0.06[e]	0.12(3)	1.74[e] $\pm$ 0.13	−0.77	0.06(2)	1.43 $\pm$ 0.11	−1.15[c]	0.10(1)	0.87[c] $\pm$ 0.11
Dy	66	1.10	0.55	0.05(2)	1.55 $\pm$ 0.09	0.00[b]	0.15(2)	1.40 $\pm$ 0.15	−0.95	0.08(4)	0.27 $\pm$ 0.12
Ho	67	0.48	−0.36	0.10(3)	1.26 $\pm$ 0.11	−0.97	0.04(4)	1.05 $\pm$ 0.08	−1.82[c]	0.11(2)	0.02[c] $\pm$ 0.11
Er	68	0.92	1.00[b]	0.11(1)	2.18 $\pm$ 0.11	0.00[b]	0.10(1)	1.58 $\pm$ 0.11	−1.20	0.10(1)	0.20 $\pm$ 0.12
Tm	69	0.10	−0.10	0.10(1)	1.90 $\pm$ 0.13	−0.75[c]	0.04(3)	1.65[c] $\pm$ 0.09	−1.85	0.10(2)	0.37 $\pm$ 0.13
Yb	70	0.84	0.70	0.10(1)	1.96 $\pm$ 0.14	−0.50[c]	0.10(1)	1.16[c] $\pm$ 0.14	−1.20[c]	0.10(1)	0.28[c] $\pm$ 0.14
Lu	71	0.10	0.20[c]	0.10(1)	2.20 $\pm$ 0.10	−0.70[c]	0.10(1)	1.70[c] $\pm$ 0.10	−0.10[e]	0.10(1)	2.12[e] $\pm$ 0.10
Hf	72	0.85	0.85	0.10(2)	2.10 $\pm$ 0.14	0.45[c,b]	0.10(1)	2.10[c] $\pm$ 0.10	−0.65	0.10(1)	0.82 $\pm$ 0.15
Ta	73	−0.12	0.70[c]	0.15(2)	2.92[c] $\pm$ 0.14	−0.20[e]	0.10(2)	2.42[e] $\pm$ 0.11	...	...	...
Os	76	1.40	1.80[e]	0.10(1)	2.50[e] $\pm$ 0.15	0.70	0.10(1)	1.80 $\pm$ 0.15	−0.15[b]	0.10(1)	0.77 $\pm$ 0.12
Ir	77	1.38	1.80[e]	0.10(1)	2.52[e] $\pm$ 0.13	...	...	...	1.30[d]	0.10(1)	0.92[d] $\pm$ 0.13

			CS 22942−019			CS 30322−023			HD 187861		
	Z	$\log_{\odot}\epsilon$[a]	log ϵ	σ_t(N)	[X/Fe] $\pm$ σ_t	log ϵ	σ_t(N)	[X/Fe] $\pm$ σ_t	log ϵ	σ_t(N)	[X/Fe] $\pm$ σ_t
Gd	64	1.07	−0.63[b]	0.12(3)	0.80 $\pm$ 0.16	−2.10[b]	0.10(1)	0.18 $\pm$ 0.17	0.15[b]	0.12(3)	1.68 $\pm$ 0.16
Tb	65	0.30	−0.60[c]	0.10(1)	1.60[c] $\pm$ 0.11	−2.00[e]	0.10(1)	1.05 $\pm$ 0.15	−1.12[c]	0.10(2)	1.18[c] $\pm$ 0.13
Dy	66	1.10	−0.65[b]	0.10(1)	0.75 $\pm$ 0.14	−1.45	0.10(1)	0.80 $\pm$ 0.13	−0.37	0.06(3)	1.13 $\pm$ 0.13
Ho	67	0.48	−1.30	0.10(1)	0.72 $\pm$ 0.14	−2.30[c]	0.10(1)	0.57[c] $\pm$ 0.14	−1.15[c]	0.07(2)	0.97[c] $\pm$ 0.09
Er	68	0.92	−0.60[b]	0.12(2)	0.98 $\pm$ 0.12	−1.50[b]	0.10(1)	0.93 $\pm$ 0.11	0.00[b]	0.10(1)	1.68 $\pm$ 0.12
Tm	69	0.10	−1.30[c]	0.10(2)	1.10[c] $\pm$ 0.11	...	...	...	−1.05	0.05(2)	1.45 $\pm$ 0.10
Yb	70	0.84	−0.70[c]	0.10(1)	0.96[c] $\pm$ 0.14	−1.90	0.10(1)	0.61 $\pm$ 0.14	−0.60[c]	0.10(1)	1.16[c] $\pm$ 0.14
Lu	71	0.10	−0.80[e]	0.10(1)	1.60[e] $\pm$ 0.10	−1.60[e]	0.10(1)	1.65[e] $\pm$ 0.10	−1.00[d]	0.10(1)	1.50[d] $\pm$ 0.10
Hf	72	0.85	−0.20[b]	0.10(1)	1.45 $\pm$ 0.09	−1.20[b]	0.10(1)	1.30 $\pm$ 0.12	0.10[b]	0.10(1)	1.85 $\pm$ 0.10
Ta	73	−0.12	−0.70[e]	0.10(1)	1.92[e] $\pm$ 0.13	−0.76[c]	0.12(3)	2.71[c] $\pm$ 0.11	−0.30[e]	0.10(2)	2.42[e] $\pm$ 0.11
Os	76	1.40	...	...	...	−0.90[e]	0.10(1)	1.05[e] $\pm$ 0.15	0.60[b]	0.10(1)	1.80 $\pm$ 0.12
Ir	77	1.38	1.60[d]	0.10(2)	2.72[d] $\pm$ 0.13	1.40[d]	0.05(2)	3.37[d] $\pm$ 0.11	1.20[d]	0.10(1)	2.42[d] $\pm$ 0.13

			HD 26			HD 55496			HD 196944		
	Z	$\log_{\odot}\epsilon$[a]	log ϵ	σ_t(N)	[X/Fe] $\pm$ σ_t	log ϵ	σ_t(N)	[X/Fe] $\pm$ σ_t	log ϵ	σ_t(N)	[X/Fe] $\pm$ σ_t
Gd	64	1.07	1.00[c,b]	0.10(1)	0.91[c] $\pm$ 0.17	−0.70[b]	0.10(1)	0.33 $\pm$ 0.17	−1.10	0.12(3)	0.33 $\pm$ 0.13
Tb	65	0.30	0.30	0.10(1)	0.98 $\pm$ 0.12	−0.66[c]	0.20(2)	1.14[c] $\pm$ 0.24	−0.60[e]	0.05(2)	1.60[e] $\pm$ 0.11
Dy	66	1.10	1.60[b]	0.10(1)	1.48[c] $\pm$ 0.15	−0.70[b]	0.10(2)	0.30 $\pm$ 0.13	−0.60[b]	0.10(2)	0.80 $\pm$ 0.15
Ho	67	0.48	0.23	0.06(2)	0.73 $\pm$ 0.11	−1.30[c]	0.10(1)	0.32[c] $\pm$ 0.14	−2.00	0.10(1)	0.02 $\pm$ 0.11
Er	68	0.92	1.60	0.10(2)	1.66 $\pm$ 0.12	−0.48[c]	0.13(2)	0.70[c] $\pm$ 0.14	−0.50[b]	0.10(1)	1.08 $\pm$ 0.11
Tm	69	0.10	0.50	0.10(1)	1.38 $\pm$ 0.13	−0.40[c]	0.10(1)	1.60[c] $\pm$ 0.13	−1.60	0.10(1)	0.80 $\pm$ 0.13
Yb	70	0.84	...	...	...	−1.00[c]	0.10(1)	0.26[c] $\pm$ 0.14	−1.05	0.10(1)	0.61 $\pm$ 0.14
Lu	71	0.10	0.40[d]	0.10(1)	1.28[d] $\pm$ 0.10	0.50[d]	0.10(1)	2.50[d] $\pm$ 0.10	...	...	...
Hf	72	0.85	2.00[b]	0.10(1)	2.13 $\pm$ 0.12	−0.60[c,b]	0.10(1)	0.65[c] $\pm$ 0.09	−0.65	0.05(2)	1.00 $\pm$ 0.12
Ta	73	−0.12	...	...	...	...	...	...	−0.60	0.10(1)	2.02 $\pm$ 0.18
Os	76	1.40	1.30[b]	0.10(1)	0.88 $\pm$ 0.12	−0.40[c]	0.10(1)	0.30[c] $\pm$ 0.15	0.20[c]	0.10(1)	1.30[c] $\pm$ 0.15
Ir	77	1.38	...	...	...	...	...	...	...	...	...

			HD 206983			HD 224959			HD 198269		
	Z	$\log_{\odot}\epsilon$[a]	log ϵ	σ_t(N)	[X/Fe] $\pm$ σ_t	log ϵ	σ_t(N)	[X/Fe] $\pm$ σ_t	log ϵ	σ_t(N)	[X/Fe] $\pm$ σ_t
Gd	64	1.07	0.30	0.10(1)	0.23 $\pm$ 0.15	0.55[b]	0.10(1)	1.84 $\pm$ 0.17	−0.30[b]	0.10(1)	0.73 $\pm$ 0.17
Tb	65	0.30	−0.90	0.10(1)	−0.20 $\pm$ 0.24	−0.69	0.08(3)	1.37 $\pm$ 0.12	−1.42	0.15(2)	0.38 $\pm$ 0.21
Dy	66	1.10	0.40[c]	0.10(1)	0.30[c] $\pm$ 0.15	0.33	0.07(3)	1.59 $\pm$ 0.11	0.10[b]	0.14(3)	1.10 $\pm$ 0.13
Ho	67	0.48	...	...	...	−0.38[c]	0.10(2)	1.50[c] $\pm$ 0.09	−1.57[c]	0.13(4)	0.05[c] $\pm$ 0.11
Er	68	0.92	0.45	0.10(1)	0.53 $\pm$ 0.16	0.45[b]	0.10(2)	1.89 $\pm$ 0.12	−0.15[b]	0.10(1)	1.03 $\pm$ 0.12
Tm	69	0.10	...	...	...	−0.43	0.04(3)	1.83 $\pm$ 0.09	−1.45	0.03(1)	0.55 $\pm$ 0.09
Yb	70	0.84	...	...	...	...	...	...	...	...	...
Lu	71	0.10	−0.35[d]	0.10(1)	0.55[d] $\pm$ 0.10	−0.20[d]	0.35(2)	2.06[d] $\pm$ 0.35	−0.32[d]	0.35(2)	1.68[d] $\pm$ 0.35
Hf	72	0.85	0.61	0.10(2)	0.76 $\pm$ 0.16	0.70[b]	0.10(2)	2.21 $\pm$ 0.09	0.10[b]	0.10(2)	1.35 $\pm$ 0.09
Ta	73	−0.12	...	...	...	−0.25[c]	0.10(1)	2.23[c] $\pm$ 0.13	...	...	...
Os	76	1.40	...	...	...	0.85[b]	0.10(1)	1.81 $\pm$ 0.12	−0.15[b]	0.10(1)	0.55 $\pm$ 0.11
Ir	77	1.38	1.30[d]	0.10(1)	0.92[d] $\pm$ 0.13	1.60[d]	0.43(2)	2.58[d] $\pm$ 0.43	0.80[d]	0.10(1)	1.52[d] $\pm$ 0.13

Notes.
[a] M. Asplund et al. (2009).
[b] D. Karinkuzhi et al. (2021).
[c] Uncertain abundances due to noisy/blended region.
[d] Very uncertain abundances due to noisy/blended region.
[e] Upper limit and uncertain.

Appendix C
Comparison with AGB model predictions

Comparison of the elemental abundances with theoretical model calculations using STAREVOL code for 1 and 2 $M_{\odot}$ AGB stars are presented in Figure C1.

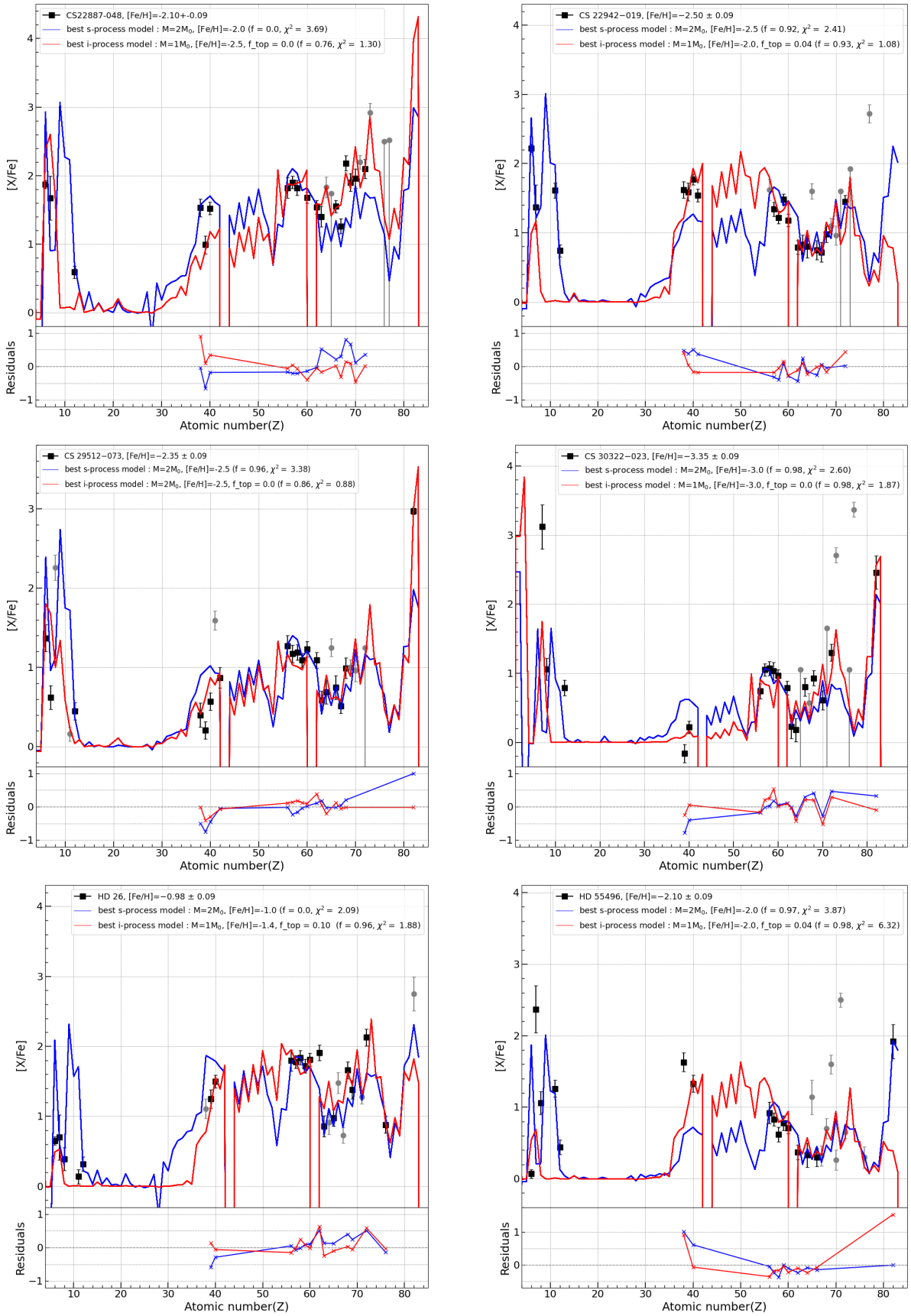

Figure C1. The abundance patterns of the 17 CEMP stars are compared with nucleosynthesis predictions from the STAREVOL code. The determined abundances are indicated by black squares, uncertain abundances by gray circles, and upper limits by gray circles with downward-pointing tails. In all cases, the best-fitting theoretical predictions for both the *s*-process (blue) and *i*-process (red) are displayed. Models are described in Section 6.

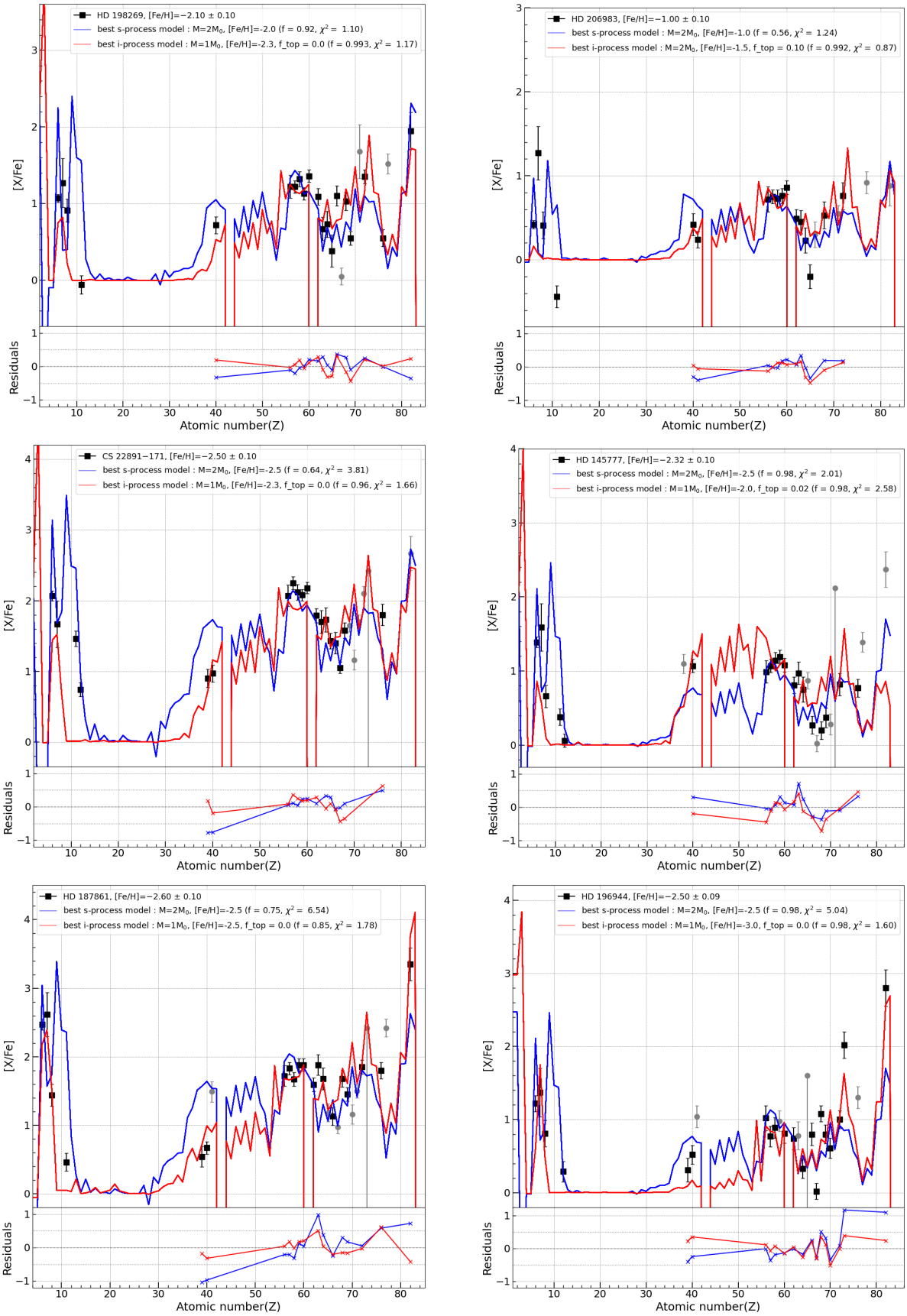

Figure C1. (Continued.)

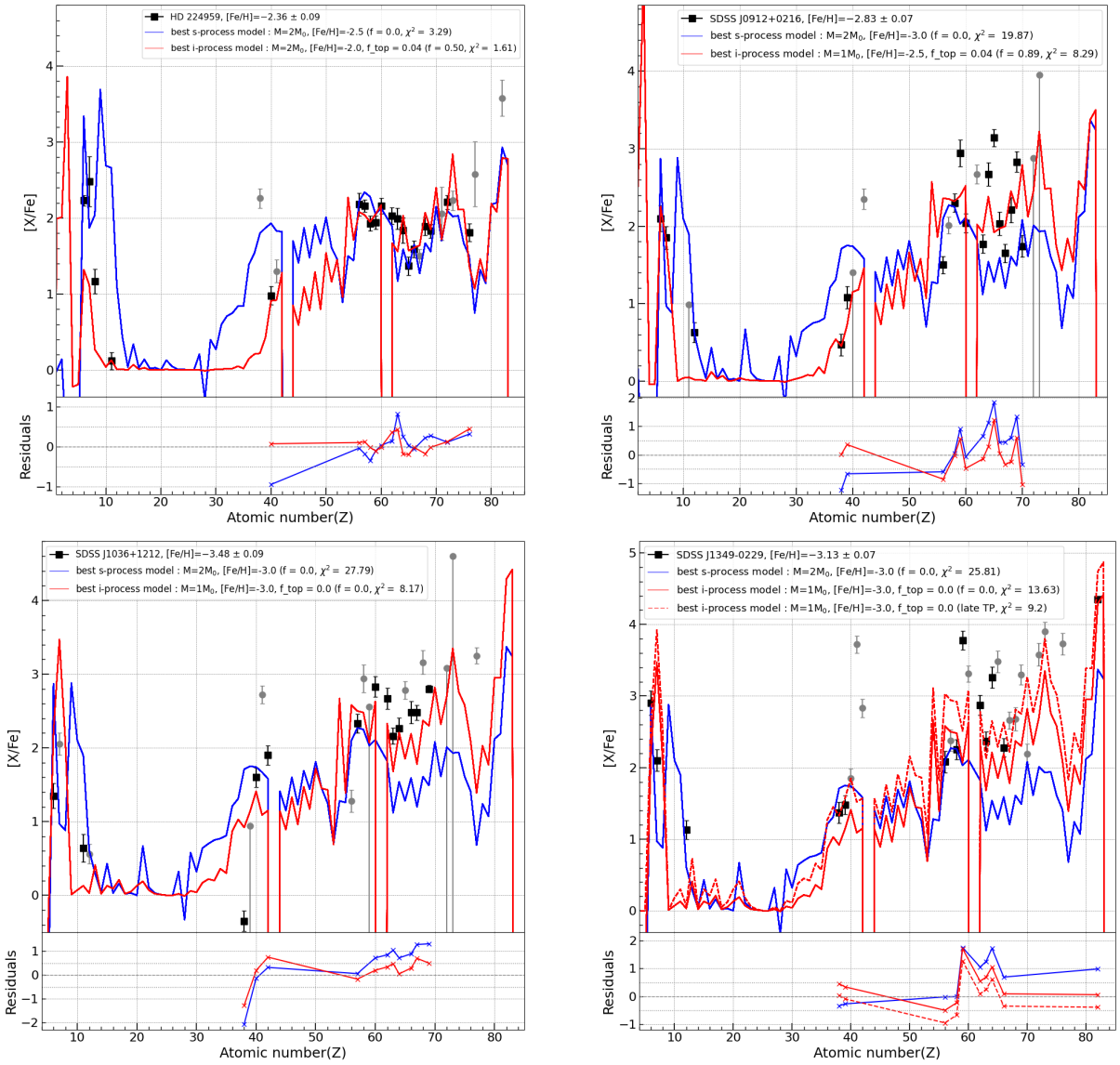

Figure C1. (Continued.)

ORCID iDs

A. M. Riyas https://orcid.org/0009-0000-1753-2212
D. Karinkuzhi https://orcid.org/0000-0002-3532-2793
S. Van Eck https://orcid.org/0000-0003-0499-8608
A. Choplin https://orcid.org/0000-0001-6159-8470
S. Goriely https://orcid.org/0000-0002-9110-941X
L. Siess https://orcid.org/0000-0001-6008-1103
M. V. Keerthy https://orcid.org/0009-0000-6607-9258
A. Jorissen https://orcid.org/0000-0002-1883-4578
T. Merle https://orcid.org/0000-0001-8253-1603

References

Abate, C., Pols, O. R., Izzard, R. G., & Karakas, A. I. 2015, A&A, 581, A22
Abate, C., Pols, O. R., Izzard, R. G., Mohamed, S. S., & de Mink, S. E. 2013, A&A, 552, A26
Abate, C., Stancliffe, R. J., & Liu, Z.-W. 2016, A&A, 587, A50
Abbott, B. P., Abbott, R., Abbott, T. D., et al. 2017, ApJL, 850, L39
Ahn, C. P., Alexandroff, R., Allende Prieto, C., et al. 2012, ApJS, 203, 21
Alexeeva, S., Ryabchikova, T., Mashonkina, L., & Hu, S. 2018, ApJ, 866, 153
Alexeeva, S., Wang, Y., Zhao, G., et al. 2023, ApJ, 957, 10
Alvarez, R., & Plez, B. 1998, A&A, 330, 1109
Aoki, W., Beers, T. C., Lee, Y. S., et al. 2013, AJ, 145, 13
Asplund, M., Grevesse, N., Sauval, A. J., & Scott, P. 2009, ARA&A, 47, 481
Beers, T. C., Chiba, M., Yoshii, Y., et al. 2000, AJ, 119, 2866
Beers, T. C., & Christlieb, N. 2005, ARA&A, 43, 531
Beers, T. C., Preston, G. W., & Shectman, S. A. 1992, AJ, 103, 1987
Behara, N. T., Bonifacio, P., Ludwig, H. G., et al. 2010, A&A, 513, A72
Bergemann, M., Hansen, C. J., Bautista, M., & Ruchti, G. 2012, A&A, 546, A90
Bisterzo, S., Gallino, R., Straniero, O., Cristallo, S., & Käppeler, F. 2011, MNRAS, 418, 284
Bisterzo, S., Gallino, R., Straniero, O., Cristallo, S., & Käppeler, F. 2012, MNRAS, 422, 849
Bonifacio, P., Monaco, L., Salvadori, S., et al. 2021, A&A, 651, A79
Buder, S., Sharma, S., Kos, J., et al. 2021, MNRAS, 506, 150
Busso, M., Gallino, R., & Wasserburg, G. J. 1999, ARA&A, 37, 239
Cescutti, G. 2008, A&A, 481, 691
Cescutti, G., Chiappini, C., Hirschi, R., Meynet, G., & Frischknecht, U. 2013, A&A, 553, A51
Charbonnel, C. 1994, A&A, 282, 811
Choplin, A., Hirschi, R., Meynet, G., et al. 2018, A&A, 618, A133
Choplin, A., Siess, L., & Goriely, S. 2021, A&A, 648, A119
Choplin, A., Siess, L., & Goriely, S. 2022a, A&A, 667, A155
Choplin, A., Siess, L., & Goriely, S. 2022b, A&A, 662, C3
Choplin, A., Siess, L., & Goriely, S. 2024a, A&A, 691, L7
Choplin, A., Siess, L., Goriely, S., & Martinet, S. 2024b, Galax, 12, 66

Choplin, A., Siess, L., Goriely, S., & Martinet, S. 2024c, A&A, 684, A206
Cowan, J. J., & Rose, W. K. 1977, ApJ, 212, 149
Cristallo, S., Straniero, O., Gallino, R., et al. 2009, ApJ, 696, 797
Cunha, K., Smith, V. V., Hasselquist, S., et al. 2017, ApJ, 844, 145
De Smedt, K., Van Winckel, H., Karakas, A. I., et al. 2012, A&A, 541, A67
Denissenkov, P., Herwig, F., Woodward, P., et al. 2019, MNRAS, 488, 4258
Denissenkov, P. A., Herwig, F., Battino, U., et al. 2017, ApJL, 834, L10
Drout, M. R., Piro, A. L., Shappee, B. J., et al. 2017, Sci, 358, 1570
Farouqi, K., Hallmann, O., Kratz, K. L., & Ott, U. 2010, in Proceedings of the 11th Symposium on Nuclei in the Cosmos (SISSA), 81
Freiburghaus, C., Rosswog, S., & Thielemann, F. K. 1999, ApJL, 525, L121
Frischknecht, U., Hirschi, R., Pignatari, M., et al. 2016, MNRAS, 456, 1803
Gaia Collaboration, Vallenari, A., Brown, A. G. A., et al. 2023, A&A, 674, 22
Gaia Collaboration 2022, yCat, 1355
Goriely, S. 1999, A&A, 342, 881
Goriely, S., Bauswein, A., & Janka, H.-T. 2011, ApJL, 738, L32
Goriely, S., & Siess, L. 2018, A&A, 609, A29
Goriely, S., Siess, L., & Choplin, A. 2021, A&A, 654, A129
Goswami, P. P., & Goswami, A. 2020, JApA, 41, 47
Gull, M., Frebel, A., Cain, M. G., et al. 2018, ApJ, 862, 174
Gustafsson, B., Edvardsson, B., Eriksson, K., et al. 2008, A&A, 486, 951
Hampel, M., Karakas, A. I., Stancliffe, R. J., Meyer, B. S., & Lugaro, M. 2019, ApJ, 887, 11
Hampel, M., Stancliffe, R. J., Lugaro, M., & Meyer, B. S. 2016, ApJ, 831, 171
Hansen, C. J., Hansen, T. T., Koch, A., et al. 2019, A&A, 623, A128
Hansen, C. J., Montes, F., & Arcones, A. 2014, ApJ, 797, 123
Hansen, T. T., Holmbeck, E. M., Beers, T. C., et al. 2018, ApJ, 858, 92
Heiter, U., Lind, K., Bergemann, M., et al. 2021, A&A, 645, A106
Heiter, U., Lind, K., Asplund, M., et al. 2015, PhyS, 90, 054010
Herwig, F., Pignatari, M., Woodward, P. R., et al. 2011, ApJ, 727, 89
Ishimaru, Y., Wanajo, S., Prantzos, N., Aoki, W., & Ryan, S. G. 2004, in The *r*-Process. The Astrophysical Origin of the Heavy Elements and Related Rare Isotope Accelerator Physics, ed. Y.-Z. Qian et al. (World Scientific), 138
Ivans, I. I., Simmerer, J., Sneden, C., et al. 2006, ApJ, 645, 613
Iwamoto, N., Kajino, T., Mathews, G. J., Fujimoto, M. Y., & Aoki, W. 2004, ApJ, 602, 377
Johnson, J. A. 2002, ApJS, 139, 219
Jonsell, K., Barklem, P. S., Gustafsson, B., et al. 2006, A&A, 451, 651
Jorissen, A., Van Eck, S., Van Winckel, H., et al. 2016, A&A, 586, A158
Jorissen, A., Začs, L., Udry, S., Lindgren, H., & Musaev, F. A. 2005, A&A, 441, 1135
Käppeler, F., Gallino, R., Bisterzo, S., & Aoki, W. 2011, RvMP, 83, 157
Karinkuzhi, D., Van Eck, S., Goriely, S., et al. 2021, A&A, 645, A61
Karinkuzhi, D., Van Eck, S., Goriely, S., et al. 2023, A&A, 677, A47
Karinkuzhi, D., Van Eck, S., Jorissen, A., et al. 2018, A&A, 618, A32
Lattimer, J. M., Mackie, F., Ravenhall, D. G., & Schramm, D. N. 1977, ApJ, 213, 225
Lee, Y. S., Beers, T. C., Kim, Y. K., et al. 2017, ApJ, 836, 91
Limberg, G., Rossi, S., Beers, T. C., et al. 2021, ApJ, 907, 10
Limongi, M., & Chieffi, A. 2018, ApJS, 237, 13
Lucatello, S., Beers, T. C., Christlieb, N., et al. 2006, ApJL, 652, L37
Lugaro, M., Campbell, S. W., & de Mink, S. E. 2009, PASA, 26, 322
Lugaro, M., Karakas, A. I., Stancliffe, R. J., & Rijs, C. 2012, ApJ, 747, 2
Martin, D., Perego, A., Arcones, A., et al. 2015, ApJ, 813, 2
Martinet, S., Choplin, A., Goriely, S., & Siess, L. 2024, A&A, 684, A8
Mashonkina, L., & Christlieb, N. 2014, A&A, 565, A123
Mashonkina, L., Pakhomov, Y., Sitnova, T., et al. 2023, MNRAS, 524, 3526
Mashonkina, L., Ryabtsev, A., & Frebel, A. 2012, A&A, 540, A98
Mashonkina, L., Zhao, G., Gehren, T., et al. 2008, A&A, 478, 529
Masseron, T., Johnson, J. A., Plez, B., et al. 2010, A&A, 509, A93
Masseron, T., Merle, T., & Hawkins, K., 2016 BACCHUS: Brussels Automatic Code for Characterizing High accUracy Spectra, Astrophysics Source Code Library, ascl:1605.004
Mathews, G. J., & Cowan, J. J. 1990, Natur, 345, 491
McClure, R. D., & Woodsworth, A. W. 1990, ApJ, 352, 709
McWilliam, A., Preston, G. W., Sneden, C., & Searle, L. 1995, AJ, 109, 2757
Nishimura, N., Sawai, H., Takiwaki, T., Yamada, S., & Thielemann, F. K. 2017, ApJL, 836, L21
Nishimura, N., Takiwaki, T., & Thielemann, F.-K. 2015, ApJ, 810, 109
Pereira, C. B., Drake, N. A., & Roig, F. 2019, MNRAS, 488, 482
Placco, V. M., Frebel, A., Beers, T. C., & Stancliffe, R. J. 2014, ApJ, 797, 21
Prantzos, N., Abia, C., Limongi, M., Chieffi, A., & Cristallo, S. 2018, MNRAS, 476, 3432
Preston, G. W., & Sneden, C. 2001, AJ, 122, 1545
Riyas, M., Karinkuzhi, D., & Van Eck, S. 2024, BSRSL, 93, 453
Rizzuti, F., Cescutti, G., Matteucci, F., et al. 2021, MNRAS, 502, 2495
Roederer, I. U., Preston, G. W., Thompson, I. B., et al. 2014, AJ, 147, 136
Rossi, S., Beers, T. C., & Sneden, C. 1999, in ASP Conf. Ser. 165, The Third Stromlo Symposium: The Galactic Halo, ed. B. K. Gibson, R. S. Axelrod, & M. E. Putman (ASP), 264
Siegel, D. M., Barnes, J., & Metzger, B. D. 2019, Natur, 569, 241
Siess, L., & Arnould, M. 2008, A&A, 489, 395
Siess, L., Dufour, E., & Forestini, M. 2000, A&A, 358, 593
Sneden, C., Cowan, J. J., & Gallino, R. 2008, ARA&A, 46, 241
Sneden, C., Cowan, J. J., Lawler, J. E., et al. 2003, ApJ, 591, 936
Thielemann, F. K., Eichler, M., Panov, I. V., & Wehmeyer, B. 2017, ARNPS, 67, 253
Watson, D. 2019, in The Extragalactic Explosive Universe: the New Era of Transient Surveys and Data-Driven Discovery, v1, Zenodo, doi:10.5281/zenodo.347811459
Wehmeyer, B., Pignatari, M., & Thielemann, F. K. 2015, MNRAS, 452, 1970
Westin, J., Sneden, C., Gustafsson, B., & Cowan, J. J. 2000, ApJ, 530, 783
Wheeler, J. C., Cowan, J. J., & Hillebrandt, W. 1998, ApJL, 493, L101
Winteler, C., Käppeli, R., Perego, A., et al. 2012, ApJL, 750, L22
Yoon, J., Beers, T. C., Placco, V. M., et al. 2016, ApJ, 833, 20